Deformation-induced melting in the margins of the West-Antarctic ice streams

Jenny Suckale[1], John D. Platt[1], Thibaut Perol,[1], and James R. Rice[1,2]

Abstract. Maps of the surface velocity of ice in West Antarctica show that flow localizes in narrow bands of fast flowing ice streams bordered by ridges of nearly stagnant ice. Despite the importance of ice streams for the stability of the West-Antarctic Ice Sheet, our understanding of the physical processes that determine their flow speed and width is incomplete. Here, we study the thermal and mechanical properties of ice-stream margins, where flow transitions from rapid to stagnant over a few kilometers. Our goal is to explore under which conditions the intense shear deformation in active ice-stream margins may lead to deformation-induced melting. We propose a 2D model that represents a cross-section through the ice-stream margin perpendicular to the downstream flow direction. We include advection and surface crevassing into our model. To estimate melt rates based on latent heat, we limit temperature by melting conditions. We strive for a realistic description of the rheology of ice entailing multiple deformation mechanisms dominant at different stresses and accounting for the temperature dependence of material properties. Using rheology parameters as constrained by laboratory data and observations, we are able to verify predictions that a zone of temperate ice is likely to form in active shear margins.

1. Introduction

The West-Antarctic Ice Sheet is thought to lose over 80% of its mass [*Bamber et al.*, 2000] through outlet glaciers and arterial drainage routes called ice streams, which are typically about a kilometer thick, tens of kilometers wide and hundreds of kilometers long. Contrary to outlet glaciers, which flow through mountain gaps and are thus confined by the topography of the land surface, topography can not fully explain the location of the fast-flowing ice streams in the Ross Ice Shelf, Antarctica [*Shabtaie and Bentley*, 1988, 1987]. Further evidence that ice-stream width is not controlled by topography alone comes from evidence that some margins have shifted in the past [*Clarke et al.*, 2000; *Fahnestock et al.*, 2000; *Jacobel et al.*, 2000, 1996] or are migrating currently [*Echelmeyer and Harrison*, 1999; *Bindschadler and Vornberger*, 1998; *Harrison et al.*, 1998]. These observations suggest that a physical mechanism must exist that allows the bed to transition from deforming beneath the ice stream to undeforming beneath the ridge, thus selecting the location of the margin and the flow speed of the stream self-consistently.

The Ross Ice Streams rest on weak and unconsolidated sediment, commonly referred to as till, which overlays former seafloor [*Tulaczyk et al.*, 1998; *Dreimanis*, 1988]. Over the last few years it has become increasingly clear that till deformation is probably the primary mechanism that allows ice streams to move rapidly despite relatively small gravitational stresses [*Alley et al.*, 1986]. In sustained flow, glacial till can be approximated as a Coulomb plastic material with a shear strength that is proportional to the effective pressure, defined as the difference between overburden and pore pressure [*Tulaczyk et al.*, 2000; *Iverson et al.*, 1998; *Kamb*, 1991]. The deformational behavior of till suggests that ice is flowing fast where the stresses in the till have reached the yielding point and is stagnant where the till is not stressed sufficiently to deform. Hence, the position of the shear margin is determined by the location where the stress in the till layer starts dropping below the yield stress of the till.

Drilling into several active ice streams has confirmed near-lithostatic fluid pressure in the till below the ice streams [*Kamb*, 2001, 1991] and inverse methods have shown that the till layer is nearly everywhere weak *Joughin et al.* [2004]. These findings imply that only a very modest shear stress can be supported by the bed. Measurements of shear stresses in the margins of the Ross Ice Streams [*Joughin et al.*, 2002] and a laboratory study of ice cores retrieved from depth [*Jackson and Kamb*, 1997] confirmed that the remainder of the driving stress is balanced by stresses on an approximately vertical surface parallel to the edge of the ice stream. We refer to these lateral boundaries of ice streams, where the surface velocity drops by two to three orders of magnitude over as little as a few kilometers, as the shear margins.

While force-balance considerations explain why shear margins play an important role in ice-stream dynamics [*Joughin et al.*, 2004; *Whillans and Van der Veen*, 2001; *Harrison et al.*, 1998; *Jackson and Kamb*, 1997; *Whillans and Van Der Veen*, 1993], they do not offer any direct insights into the mechanism through which the margin affects the ice-stream flow. One possibility is that shear margins represent not only the transition from fast to slow flow, but may also coincide with the boundary between temperate and frozen conditions at the bed [*Schoof*, 2012; *Jacobson and Raymond*, 1998]. One challenge with this idea is that even a small perturbation in ice-stream width would lead to either run-away growth or to stoppage of an ice stream [*Jacobson and Raymond*, 1998]. *Schoof* [2004] questioned the assumption that the transition between a temperate and a frozen bed determines, or even coincides with, the position of the shear margin. Instead, he invokes a spatially variable yield stress in the till layer, analogous to Barenblatt-Dugdale concepts in fracture mechanics (e.g., *Rice* [1968a, b]), and derives the associated stream widths. However, *Schoof* [2004]

[1]School of Engineering and Applied Sciences, Harvard University, Cambridge, Massachusetts, USA.

[2]Department of Earth and Planetary Sciences, Harvard University, Cambridge, Massachusetts, USA.

0148-0227/13/$9.00

assumes a Newtonian rheology, recognized as a severe simplification, and does not offer an explanation for the assumed functional forms of the yield stress along the glacial bed.

The goal of this study is to investigate the possibility of deformation-induced melting in active shear margins. There are two reasons why melting and the associated presence of meltwater in ice-stream margins might have important consequences for the dynamics of ice streams. First, the shear strength of glacial till varies highly with porosity, which is controlled by the water content for full saturation [*Rathbun et al.*, 2008; *Tulaczyk*, 1999; *Iverson et al.*, 1998] and diminishes with effective pressure, in agreement with critical-state soil mechanics (e.g., *Schofield and Wroth* [1968]). The sensitive dependence of shear strength on water content suggests that the spatial variability of basal stress and the positions of the shear margins could be intricately linked to meltwater generation. Second, if significant quantities of meltwater are produced in the margin, the water may accumulate in a channelized drainage system as pointed out by *Perol and Rice* [2011]. The presence of a channel alters both the basal stresses outside of it and the pore-pressure distribution in its vicinity, which could contribute to locking of the bed of a widening stream.

The possibility that the shear margins of active ice streams may be temperate was first pointed out by *Jacobson and Raymond* [1998] and studied in more detail by *Beem et al.* [2010] and *Perol and Rice* [2011]. Assuming uniform strain rates through the ice thickness, *Perol and Rice* [2011] devised a 1D heat-transfer model, which, however, was not versatile enough to allow for ice advection perpendicular to the margin. They showed that the shear-strain rates measured by [*Joughin et al.*, 2002] for the five Ross Ice Streams are consistent with internal melting at depth for all stream margins except the currently inactive Kamb Ice Stream. As remarked upon by *Perol and Rice* [2013], there is also some observational evidence suggesting a temperate zone. *Clarke et al.* [2000] combined different radar measurements to image the ice sheet in the vicinity of Unicorn ridge (Figure 1). They found numerous linear diffractors near the base of the ice sheet, some of which *Clarke et al.* [2000] interpreted as entrained morainal debris. One prominent feature in their study is a bottom diffractor that extends to about 230 m above the bed and might delineate a zone of wet and reflective ice [*Clarke et al.*, 2000]. Further, drilling into the currently inactive Kamb ice stream margin revealed flowing water in a 1.6 m cavity between the bottom of the ice sheet and its bed [*Vogel et al.*, 2005].

Here, we devise a 2D thermomechanical model of an ice stream moving over a plastic bed in steady state. We consider a cross-section through the ice-stream margin perpendicular to the downstream flow direction and analyze the effect of the anti-plane shear stress components on the mechanical equilibrium and energy dissipation. Our ice rheology takes multiple creep mechanisms into account, which dominate at different stress levels. In addition to diffusion and advection of heat, we include the temperature dependence of material properties and a simplified representation of surface crevassing assuming a temporally steady state of stress and flow velocity. To estimate melt rates based on latent heat, we limit temperature by melting conditions. We solve the governing equations numerically using finite differences for a Cartesian grid with three refinement levels. We also carefully benchmark our computational technique to demonstrate that we resolve the stress concentration and nonlinearities implied in our model setup.

Our model is intended as a representation of the Ross Ice Streams. Despite the general scope of the model, we chose the southern margin of Whillans ice stream B2, commonly referred to as Dragon margin (Figure 1), as a specific test case for our model. Dragon margin is located nearby research camps and skiways and has been studied extensively. The two most important data sets for our purposes

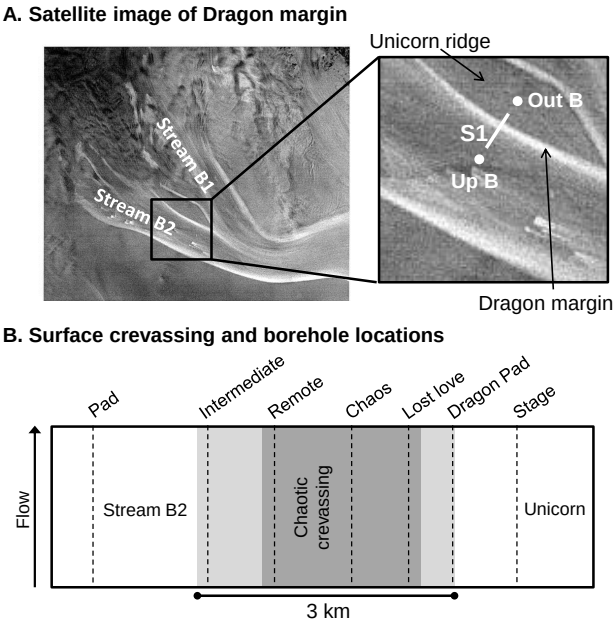

Figure 1. A: The left panel shows a satellite image of the confluence between Ice Streams B1 and B2 in the upstream portion of Whillans Ice Stream, taken by the Radarsat Antarctic Mapping Project. The right panel is a detailed view of Dragon margin, Unicorn ridge and the profile S1 along which *Echelmeyer and Harrison* [1999] measured surface velocities and *Harrison et al.* [1998] reported temperature for the upper few hundred meters. We have highlighted the positions of the two outermost boreholes, Out B and Up B, used in *Harrison et al.* [1998]. B: Approximate locations of the seven boreholes in the vicinity of the shear margin with respect to surface crevassing (after *Harrison et al.* [1998]). The dark grey area represents the roughly 2 km-wide zone of chaotic crevassing. The light grey zones exhibit less intense crevassing.

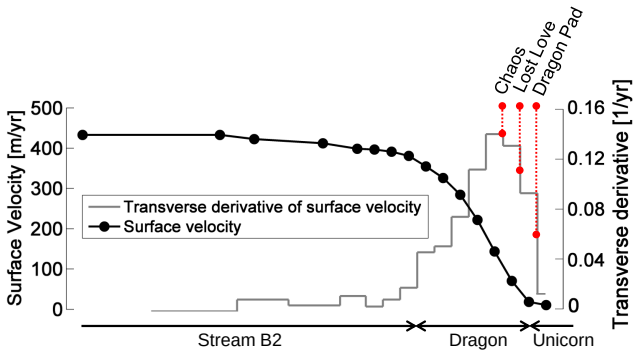

Figure 2. Surface velocities across Dragon margin as measured by *Echelmeyer and Harrison* [1999] and the transverse derivative of surface velocities, $\mathrm{d}u/\mathrm{d}y$, computed from the measured surface velocities. Highlighted in red are the approximate transverse velocity derivatives for boreholes 'Dragon Pad', 'Love Love', and 'Chaos' quoted from *Harrison et al.* [1998].

are detailed observations of surface velocities across Dragon margin [*Echelmeyer and Harrison*, 1999; *Echelmeyer et al.*, 1994] and temperature measurements from nine boreholes distributed across Dragon margin [*Harrison et al.*, 1998] (Figure. 2). In addition, *Jackson and Kamb* [1997] measured the enhancement factor at Dragon margin to fit the observed rheology with the standard parametrization of Glen's law and *Clarke et al.* [2000] provided valuable insights into the complex deformational history of the area over the last few hundred years.

2. Model setup

We consider a slab of ice flowing in the downstream direction x (Figure 3). The height coordinate, z, is taken positive upward from the base of the ice. In the transverse direction, the ice stream extends from the left boundary of the domain to its center ($-W/2 \leq y \leq 0$) and the ridge from the center to the right boundary of the domain ($0 \leq y \leq W/2$). The left boundary of our modeling domain thus coincides with the middle of the stream and the origin of our coordinate system ($y = 0$, $z = 0$) represents the transition point from slipping to locking at the bed, indicated as a black dot in Figure 3. We do not explicitly model the process which would lead to such a transition. We distinguish the locked-to-sliding transition point from the shear margin itself, which constitutes the ice column at the lateral boundary of the stream where the surface velocity of ice increases rapidly over a few kilometers. We assume negligible variation of ice-sheet thickness in the transverse direction (along the y axis) and neglect topography at the bed, such that the ice surface is parallel to the bed. We also neglect downstream variation of ice properties and flow speed u, which reduces our model to two dimensions, and assume a lithostatic pressure field. All notations used in this paper are summarized in Table 1 at the end of the paper.

2.1. Mechanical model

The only free variable of our mechanical model is the downstream velocity $u(y, z)$. Accordingly, the strain-rate tensor $\dot{\boldsymbol{\epsilon}}$,

$$\dot{\epsilon}_{ij} = \frac{1}{2}\left(\frac{\partial u_j}{\partial x_i} + \frac{\partial u_i}{\partial x_j}\right), \tag{1}$$

and the deviatoric stress tensor $\boldsymbol{\tau}$ have only two non-zero components, the shear strain rates and shear stresses in horizontal ($\dot{\epsilon}_{xy}$ and τ_{xy}) and vertical ($\dot{\epsilon}_{xz}$ and τ_{xz}) direction on a face where x is constant. Given these assumptions, the conservation of momentum (or static equilibrium in this case) reduces to

$$\frac{\partial}{\partial y}\left(\mu\frac{\partial u}{\partial y}\right) + \frac{\partial}{\partial z}\left(\mu\frac{\partial u}{\partial z}\right) + \rho g \sin\alpha = 0 \tag{2}$$

where ρ is the ice density, g is the acceleration due to gravity, α is the inclination angle of the slab, and μ is the temperature- and strain-rate-dependent, effective dynamic viscosity. Note that by reducing our analysis to anti-plane deformation as in eq. 2, we inevitably neglect small components of in-plane deformation that must accompany the marginal melting and drainage that we later infer.

The stream-ridge system in Figure 3 is underlain everywhere by a thick layer of glacial till. Underneath the ice stream, the till is failing in shear, which justifies equating the basal shear stress, τ_{base}, underneath the ice stream with the yield stress. In the interest of simplicity, we assume that the basal stress is constant. Underneath the ridge, we assume that the shear stress at the ice-till interface does not exceed the yield stress, implying that failure and sliding do not occur. The full details which explain locking are yet to be fully understood. The appropriate boundary conditions at the bed are then

$$\tau_{xz} = \tau_{base} \quad \text{at} \quad z = 0,\, y \leq 0 \tag{3}$$

$$u = 0 \quad \text{at} \quad z = 0,\, y > 0\,. \tag{4}$$

The ice surface is assumed to be stress free. On the sides of the modeling domain, we use symmetric boundary conditions, implying an infinite juxtaposition of ice streams and ridges. Later, we estimate τ_{base} to best match measured surface flow rates and borehole temperature profiles.

2.2. Ice rheology

There is no single mechanism that captures how ice deforms over a wide range of stresses [*Cuffey and Paterson*, 2010]. For our modeling domain, which encompasses both high and low stress conditions, we approximate the rheology of ice as a combination of diffusional creep $\dot{\boldsymbol{\epsilon}}_{\boldsymbol{D}}$ and Glen's Law $\dot{\boldsymbol{\epsilon}}_{\boldsymbol{G}}$

$$\dot{\boldsymbol{\epsilon}} = \dot{\boldsymbol{\epsilon}}_{\boldsymbol{D}} + \dot{\boldsymbol{\epsilon}}_{\boldsymbol{G}}\,. \tag{5}$$

Diffusional creep

$$(\dot{\epsilon}_D)_{ij} = \frac{42\Omega}{k_B T d^2} B \exp\left(-\frac{Q}{RT}\right)\tau_{ij}\,, \tag{6}$$

dominates the deformational behavior of ice at low stresses and Glen's Law

$$(\dot{\epsilon}_G)_{ij} = AE \exp\left[-\frac{Q}{R}\left(\frac{1}{T_h} - \frac{1}{T^*}\right)\right]\tau_E^2 \tau_{ij}\,, \tag{7}$$

dominates at intermediate to high stresses, where τ_E is the effective shear stress defined by the second invariant of the deviatoric stress tensor, in our case $\tau_E^2 = \tau_{xy}^2 + \tau_{xz}^2$, and $\dot{\epsilon}_E$ is the effective tensorial deviatoric strain rate, in our case $\dot{\epsilon}_E^2 = \dot{\epsilon}_{xy}^2 + \dot{\epsilon}_{xz}^2$.

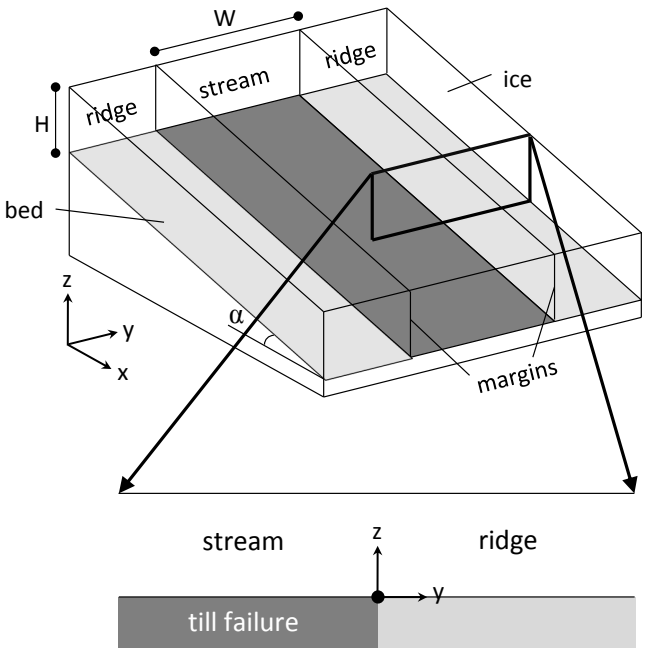

Figure 3. Simplified geometry of our model setup. The ice thickness is H and the total width of the stream is W. The 2D setup (bottom) is equivalent to assuming a 3D stream-ridge geometry with no downstream variation (top).

The parameters specifying diffusional creep in (eq. 6) are the molecular volume $\Omega = 3.27\,10^{-29}\,\mathrm{m}^3$, the Boltzmann constant $k_B = 1.38\,10^{-23}\,\mathrm{m}^2\,\mathrm{kg}\,\mathrm{s}^{-2}\,\mathrm{K}^{-1}$, the grain size d =1-10 mm, the exponential prefactor $B = 9.1\,10^{-4}\,\mathrm{m}^2\,\mathrm{s}^{-1}$, the activation energy $Q = 59.4\,\mathrm{kJ\,mol}^{-1}$, and the gas constant $R = 8.314\,\mathrm{J\,K}^{-1}\mathrm{mol}^{-1}$ [*Frost and Ashby*, 1982]. For Glen's Law (eq. 7), we follow *Cuffey and Paterson* [2010] in using the pre-exponential constant $A = 3.5\,10^{-25}\,\mathrm{s}^{-1}\mathrm{Pa}^{-3}$, the temperature adjusted for melting point depression $T_h = T + p_0 P$ with $p_0 = 7 \times 10^{-8}\,\mathrm{K\,Pa}^{-1}$ and T in K, and the activation energy $Q = 60\,\mathrm{kJ\,mol}^{-1}$ for $T_h < T^*$ and $Q = 115\,\mathrm{kJ\,mol}^{-1}$ for $T_h > T^*$ where $T^* = 263.15\,\mathrm{K} = -10°\mathrm{C}$. The sum of the coefficients of τ_{ij} in eqs. 6 and 7 defines $1/(2\mu)$.

The rheological parameter that is most difficult to constrain is the enhancement factor. Enhancement is not a physical variable by itself, but represents effects of grain size, impurities, fabrics and possibly other variables [*Cuffey and Paterson*, 2010]. As a consequence, estimates for enhancement vary widely. For the specific case of Dragon margin, *Jackson and Kamb* [1997] determined enhancement factors between $E \approx 1.12$ and $E \approx 2.55$ for different ice specimen retrieved from Dragon margin. Because of the significant ambiguity introduced into our model results even by this moderate variation, we set $E = 1$ for most of our computations to allow for easier comparisons. We discuss the ramifications of varying enhancement in Sec. 5.

2.3. Thermal model

Our thermal model captures the effect of both diffusion and advection of heat. In addition, we cap temperature at the melting point to estimate melt production based on latent heat and include the effect of cold surface air pooling in crevasses [*Harrison et al.*, 1998]. For a spatially-variable thermal conductivity k, the steady-state temperature field is thus given by

$$\frac{\partial}{\partial y}\left(k\frac{\partial T}{\partial y}\right) + \frac{\partial}{\partial z}\left(k\frac{\partial T}{\partial z}\right) + \rho c\left(v\frac{\partial T}{\partial y} + w\frac{\partial T}{\partial z}\right) + 2\tau_E\dot{\epsilon}_E - L\dot{m} = 0\,, \qquad (8)$$

where v and w are the lateral and vertical advection speeds, respectively, c is the specific heat of ice, τ_E is the effective shear stress, $\dot{\epsilon}_E$ is the effective tensorial shear strain rate, L is the latent heat of ice per unit mass and $\dot{m}$ is the mass melting per unit time and unit volume. The thermal conductivity k and specific heat c vary with temperature as summarized in *Cuffey and Paterson* [2010]:

$$k(T) = k_1\,\exp(-k_2 \times 10^{-3}\,T) \qquad (9)$$

$$c(T) = c_1 + c_2\,T\,, \qquad (10)$$

where T is in Kelvin and the forefactors are $k_1 = 9.828\,\mathrm{W\,m}^{-1}\,\mathrm{K}^{-1}$, $k_2 = 5.7\,\mathrm{K}^{-1}$, $c_1 = 152.5\,\mathrm{J\,kg}^{-1}\,\mathrm{K}^{-1}$, and $c_2 = 7.122\,\mathrm{J\,kg}^{-1}\,\mathrm{K}^{-2}$, respectively.

To compute the melt rate per unit volume $\dot{m}$ in eq. 8, we assume that shear heating in the temperate zone is absorbed as latent heat. This assumption implies that the temperature in the temperate zone is capped at the melting point, which allows us to reduce eq. 8 to the following non-linear Poisson problem

$$\frac{\partial}{\partial y}\left(k\frac{\partial T}{\partial y}\right) + \frac{\partial}{\partial z}\left(k\frac{\partial T}{\partial z}\right) + \rho c\left(v\frac{\partial T}{\partial y} + w\frac{\partial T}{\partial z}\right) + [1 - H(T - T_m)]\,2\tau_E\dot{\epsilon}_E = 0\,, \qquad (11)$$

where $H(T-T_m)$ denotes the Heaviside function. $H(T-T_m)$ is one in the temperate zone and zero outside such that $L\dot{m}$ is non-zero only in the temperate zone where it equals the shear heating $2\tau_E\dot{\epsilon}_E$.

The mechanical model set up in Section 2.1 solves only for the downstream velocity u. To include the horizontal and vertical velocities into our thermal model, we constrain the functional forms for both v and w apriori, assuming that the associated strain rates, stresses and work rates are negligible. Considering horizontal and vertical velocities in the thermal but not the mechanical model is, of course, strictly inconsistent. This inaccuracy is warranted by the potentially important effect that the advection of cold ice into the shear margin is likely to have on deformation-induced melting [*Jacobson and Raymond*, 1998]. In the mechanical model, however, the strain rates associated with the horizontal and vertical velocities are two orders of magnitude smaller than the anti-plane rates, implying that the strain rate components in these directions can be neglected in $\dot{\epsilon}_E$ of the creep law and the equilibrium equation.

For the vertical advection component we follow *Zotikov* [1986] and *Jacobson and Raymond* [1998] in assuming that w varies linearly with depth

$$w(y,z) = -a\frac{z}{H}\,, \qquad (12)$$

where a is the surface accumulation rate of ice in m/yr and a uniform contribution to w equal to the melt rate at the bed of the ice sheet is neglected. Eq. 12 implies that accumulation of ice at the surface is compensated by downslope stretching of ice and that basal melting or freeze-on are negligible [*Zotikov*, 1986].

Several studies have suggested that the position of Dragon margin has shifted in the past and may even be shifting currently with speeds on the order of 1-10 m/yr [*Echelmeyer and Harrison*, 1999; *Harrison et al.*, 1998] to potentially ≈ 100 m/yr [*Clarke et al.*, 2000; *Bindschadler and Vornberger*, 1998]. The simplest way to include ongoing margin migration at constant rate into our ice-stream model is through influx of cold ice from the ridge based on the rationale that in a coordinate system moving with the margin, outward expansion of the stream is equivalent to influx of cold ice from the ridge (as also argued in *Schoof* [2012]). To be consistent with zero-slip boundary condition at the bed underneath the ridge, we impose

$$v(y,z) = v_0\left[1 - \left(\frac{H-z}{H}\right)^4\right]\,, \qquad (13)$$

(see for example *Cuffey and Paterson* [2010]).

Similarly to the mechanical model, we use symmetric boundary condition on the sides of the domain. On the top, we specify the surface temperature of ice (see Sec. 2.5). Underneath the stream, we assume that the bed is at the melting point as supported by observations (e.g. *Engelhardt et al.* [1990]). Underneath the ridge, we do not specify apriori whether the bed is temperate or not. Instead, we adjust the geothermal heat flux G directly beneath the ice sheet such that the bed reaches a temperature of $-5°\mathrm{C}$ at large distances from the margin in agreement with observations (e.g. *Rose* [1979]). Depending on the computation, this condition typically requires geothermal heat fluxes on the order of G = 48-85 $\mathrm{mW/m}^2$. We assume the same geothermal heat flux underneath the stream. Assuming a finite geothermal heat flux underneath the ice stream has no effect on the solution for the downstream velocity and temperature, because the additional heating does not raise the base temperature above the melting point. It does, however, affect the total meltwater generation associated with both the geothermal heat flux and the frictional heating at the base of the ice stream (Sec. 2.4).

2.4. Meltwater production

Despite the fact that our mechanical model (Sec. 2.1) entails a stress singularity, it is an integrable singularity from the standpoint of both force equilibrium and heat balance, which allows us to use the dissipation in the temperate zone to obtain an estimate for the melt rate per unit volume (see Sec. 2.3). In 2D, the mass balance for the meltwater produced in the temperate zone is

$$\frac{\partial q_y}{\partial y} + \frac{\partial q_z}{\partial z} = -\frac{2\tau_E \dot{\epsilon}_E}{L\rho_w} \tag{14}$$

where q_y and q_z represent the meltwater flux in horizontal and vertical direction, respectively, and ρ_w is the density of water.

For simplicity, we neglect meltwater flux in the horizontal direction, $q_y = 0$, noting that we have previously assumed a hydrostatic pressure in our mechanical model (Sec. 2.1), and integrate eq. 14 numerically to obtain the basal meltwater flux due to shear heating in the temperate zone very simply as

$$q_{temp} = -\int_0^{H_m} \frac{\dot{m}}{\rho_w} \mathrm{dz} = -\int_0^{H_m} \frac{2\tau_E \dot{\epsilon}_E}{L\rho_w} \mathrm{dz}\,, \tag{15}$$

where H_m indicates the height of the temperate zone measured from the bed upwards. In addition to melt production from shear heating in the temperate zone, frictional heat dissipation at the bed and the difference between heat in- and out-flux may contribute to the melt rate, yielding

$$q_{base} = q_{temp} + \frac{1}{L\rho_w}\left[u(y,0)\tau_{base} + G - k\frac{\partial T}{\partial z}\right]. \tag{16}$$

Based on the two assumptions that meltwater percolation occurs through Darcy's law [*Lliboutry*, 1996] and that the water pressure in veins equals the ice overburden pressure, $\mathrm{d}p/\mathrm{dz} = -\rho g$, the permeability of the temperate ice can be deduced as [*Perol and Rice*, 2011]

$$\kappa = \frac{q_{base}\mu_w}{(\rho - \rho_w)g}\,. \tag{17}$$

The meltwater fluxes we later infer imply a temperate-ice permeabilities on the order of $10^{-16}\,\mathrm{m}^2$, which is consistent with measurements by *Jordan and Stark* [2001].

2.5. Surface crevassing

The crevassed zone at Dragon margin consists of an approximately 2 km-wide zone of intense, chaotic crevassing [*Echelmeyer and Harrison*, 1999; *Harrison et al.*, 1998; *Vornberger and Whillans*, 1990]. On the ridge-side of the margin, the chaotic crevasses transition to large arcuate crevasses and on the stream-side to somewhat organized and widely spaced crevasses that tend upstream [*Echelmeyer and Harrison*, 1999; *Harrison et al.*, 1998]. The crevasses are thought to extend about 30 m into the ice [*Harrison et al.*, 1998]. The location of the crevassed zone and the positions of the nine boreholes for which *Harrison et al.* [1998] reported temperature measurements are reproduced in Fig. 1A and B. *Harrison et al.* [1998] also indicate the transverse derivatives of the surface velocities at the three boreholes, 'Dragon Pad', 'Lost Love', and 'Chaos' (Fig. 2), which indicates that borehole 'Dragon Pad' is located closest to the locked-to-sliding transition but on the ridge side, at approximately $y = 200$ in our modeling domain (Fig. 3).

We represent the zone of chaotic crevassing as a 2 km-wide rectangular area in our y, z-plane that extends from the surface 30 m into the ice. We assume that the dense spacing of open crevasses lowers the effective viscosity in this area by an order of magnitude as compared to uncrevassed ice (i.e. from μ to $\mu/10$). We refer to the drop in effective viscosity as the mechanical-weakening factor. While this choice

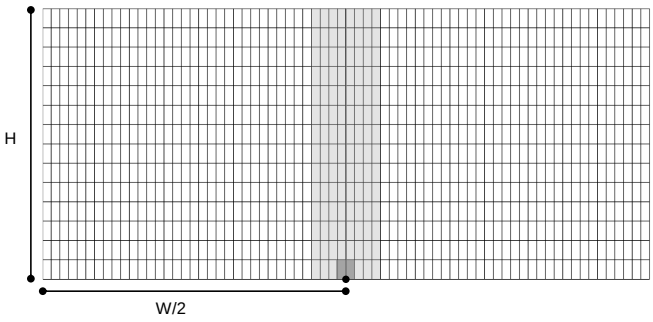

Figure 4. Cartesian grid used in our computation. The grey shaded areas highlight the two zones of grid refinement necessary to resolve the sudden transition from fast flow to stagnation at the ice-stream bed.

is somewhat arbitrary, we verified that the results are not sensitive to the assumed value, mostly because the crevassed zone is relatively shallow. To capture the zones of arcuate and upstream crevassing on the ridge and stream side of the chaotic zone, we gradually lower the effective viscosity unaffected by crevassing to the mechanically-weakened effective viscosity representative of chaotic crvassing over 400 m on both the stream and the ridge side. We include the effect of cool winter ice pooling in the crevasses by enforcing a surface temperature of -34 C° in the crevassed zone, which gradually increases to -26 C° in the uncrevassed ice.

There is no doubt that the representation of surface crevassing considered here is simplified. A more complete model would allow the crevassed zone to evolve self-consistently instead of specifying its extent apriori. Nonetheless, we argue that the approach we have chosen

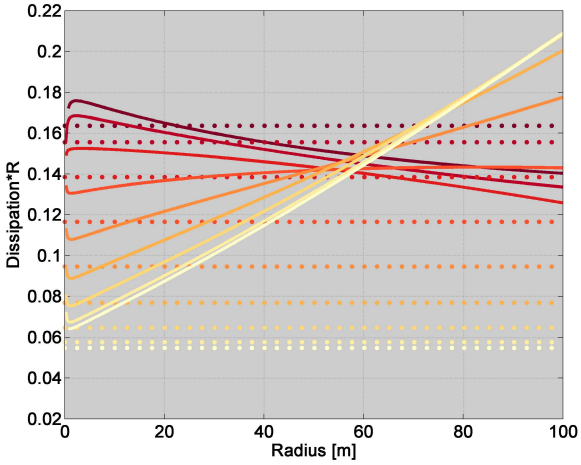

Figure 5. Benchmark computation for Dragon margin ($W = 34H$). Each color represents one of nine different angles from 5°-175°. For each angle, the dotted lines represent the analytically-derived nonsingular shear heating and the full lines the numerically-derived nonsingular shear heating. The discrepancy at $r \approx 5$ m between numerical and analytical for this specific computation is due to the analytical solution requiring $W \gg H$, which is only approximately true for ice stream B2. There is no discernible difference between our analytical and numerical estimates for very wide ice streams ($W > 200H$).

here provides a reasonable first step for considering crevassing in the context of a steady-state model.

3. Methodology

3.1. Numerical methodology

Our numerical implementation uses centered finite-differences on a Cartesian grid, yielding a second-order accurate approximation to the governing equations. Our grid setup allows for three refinement levels in the vicinity of the singularity at the transition point between stream and ridge in the mechanical model (see Section 2.1). We assess the adequacy of this grid setup through a comparison with an analytical treatment of the singularity in Sec. 4.1. We do not use grid refinement in our solution to the thermal model (see Section 2.3), because our temperature field is capped at the melting point, which implies constant temperature in the vicinity of the stress singularity.

The mechanical and thermal model are coupled through the dependence of viscosity on temperature and the dependence of temperature on shear heating. We therefore have to solve the two models iteratively by repeating the following computational steps: First, we seek an approximate solution to our mechanical model (eq. 2). Second, we compute the dissipative heating associated with the estimated velocity field. Third, we compute the temperature field resulting from this dissipative heating term by solving eq. 11. Fourth, we update our estimates for the effective viscosity, thermal conductivity and specific heat based on the new temperature field. Once the coupled mechanical and thermal models have converged to a stable solution for the temperature and velocity fields of the stream-ridge system, we estimate melt production (eq. 16).

A concern when solving our mechanical model numerically for a creep-type rheology is to resolve the singularity at the base between stream and ridge sufficiently. We ameliorate this problem by using a grid with three refinement levels in the vicinity of the singularity. It is worth mentioning at this point that while our rheology entails more parameters than a simple Glen Law, most of these parameters are not varied in our computations. We tested the impact of varying the grain size in eq. 6 within a reasonable range of 1-10 mm and found little effect. The Glen-law component of the rheology clearly dominates the thermomechanical behavior in most of the computational domain.

The main challenge in our thermal model is that the source term in eq. 11 depends on temperature, which makes the equation nonlinear. The solution of eq. 11 thus requires an iterative procedure in itself. At each iteration, we update the source term based on the revised estimate for the extent of the temperate zone. We also shift the transition between the boundary condition at the base of the domain, such that geothermal heat flux is imposed only underneath the portion of the ridge that is frozen (although we continue to maintain a no-slip condition underneath the entire ridge). We solve eq. 11 through a multigrid solver [*Briggs et al.*, 2000], in which we cycle through a sequence of four increasingly coarse grids. We have also found satisfactory results with classical iterative techniques such as successive overrelaxation, but the multigrid is computationally more efficient and less prone to error oscillations, particularly along the bed.

To specify the material properties in the crevassed zone, we construct a Heaviside distribution of 2 km width and 30 m depth, in which we reduce the effective viscosity as computed from eqs. 5-7 for the lowered temperatures in the crevassed zone by the mechanical weakening factor. We smear out the transition between chaotic crevassing and uncrevassed ice over 400 m using a standard trigonometric taper to represent the areas of less intense crevassing [*Harrison et al.*, 1998]. The crevassed zone thus has a total width of 2.8 km. We enforce a surface temperature of -34 C$^\circ$ in the crevassed zone, which gradually increases to -26 C$^\circ$ in the uncrevassed ice based on the same smeared Heaviside function.

3.2. Validation of the numerical approach

Two previous studies [*Schoof*, 2004; *Jacobson and Raymond*, 1998] have investigated the thermomechanics of ice-stream margins with differing results. While some of the differences are clearly due to contrasting model assumptions, *Schoof* [2004] raised the concern that a purely numerical approach, like *Jacobson and Raymond* [1998], might not resolve the singularity in the mechanical model. Instead, *Schoof* [2004] devised a nonsingular model like commonly used in fracture theory that can be solved analytically, but is based on significant simplifying assumptions. To relax some of these assumptions, we have developed the numerical approach described in Sec. 3.1, but validate it carefully against an analytical treatment to ensure that we resolve the singularity adequately.

Mathematically, the transition from a slipping ice stream to a locked ridge is analogous to a crack problem. In this analogy, the singularity at the bed between stream and ridge represents the crack tip and the base of the ice stream can be thought of as a shear crack. Using this parallel, we can study the dissipation in the near-tip field with the analytical techniques developed for crack mechanics. Our strategy for solving for the stress, strain-rate and dissipation in the near-tip field consists of two steps: First, we can deduce from *Rice* [1967], reinterpreted for nonlinear viscous flow, and *Rice* [1968b] that the shear heating in the near-tip region is given by

$$2\tau_E\dot{\epsilon}_E = \frac{3J_{tip}}{2\pi r}\left(\sqrt{4-\sin^2\theta}+\cos\theta\right) \tag{18}$$

where r and θ are the polar coordinates centered on the slip singularity, such that r is the radial distance from the slip singularity and θ the angle taken to be zero at the bed underneath the ridge (see appendix A for details). The $1/r$ term in this result applies for any creep law, while the angular dependence here is specific to Glen's law. Eq. 18 provides an exact solution for the shear heating in the near-field parametrized by an unspecified constant, J_{tip}. This constant, J_{tip}, captures the intensity of straining at the crack tip, which depends on the far-field loading. To create the link to the far field in the second step of our analysis, we use the path-independence of J-type integrals, which were pioneered by *Rice* [1968a], *Rice* [1968b], *Cherepanov* [1968], and *Bilby and Eshelby* [1968] in the context of cracks in elastic solids, but have been generalized to more complex, non-linear creep rheologies (e.g. *Ben Amar and Rice* [2002]; *Kubo et al.* [1979]; *Landes and Begley* [1976]; *Goldman and Hutchinson* [1975]) relevant for our case and applied to glaciers by *McMeeking and Johnson* [1986]. As detailed in appendix B, we evaluate the J-integral around the boundary of the domain, which due to path-independence allows us to approximately estimate J_{tip} as

$$J_{tip} = H\tau_{lat}\dot{\epsilon}_{lat}\,, \tag{19}$$

where τ_{lat} is the average shear stress, τ_{xy}, at the margin that would balance the gravitational load of the ice stream and $\dot{\epsilon}_{lat}$ is the strain rate associated with that average lateral shear stress. Note that contrary to the exact result for the near-tip field (see eq. 18), the evaluation of the J-integral in eq. 19 is approximate and based on the simplifying assumptions that (1) the rheological behavior of ice is independent of position, hence neglecting the effect of temperature variations and (2) that ice streams are much wider than thick ($H \ll W$). It is also worth noting that Glen's Law clearly dominates the ice rheology in the high-stress region around the crack tip, which obviates taking diffusional creep into account although the analysis procedures remain valid with it included. Also, to the extent that the near-tip zone is temperate, the first condition may be met within that zone.

4. Results

To gain a better understanding of the different effects that contribute to the thermomechanics of ice streams, we start by reducing our model to its bare minimum. In its most simplistic form, the model is reminiscent of models that are amenable to analytical solution like *Schoof* [2004]. Then, we add in one term after another, gradually obtaining a more realistic representation of the behavior of a stream-ridge system.

The sequence of effects that we consider is as follows: First, we focus on the role of the singularity at the locking-to-slipping transition point at the bed. Second, we investigate the ramifications of a temperature-dependent creep rheology. Third, we consider the ramifications of vertical and horizontal advection of cold ice into the margin. Fourth, we take into account crevasses along the surface expression of the margin. To quantify the explanatory potential of this sequence of approximations, we attempt to reproduce the surface velocities measured for Dragon margin by *Echelmeyer and Harrison* [1999] at each step and compare the respective fits.

4.1. The role of the singularity

Numerical models of singular systems are inevitably less accurate than analytical approaches in the immediate vicinity of the singularity. It is thus valuable to first verify that the singularity is resolved satisfactorily in our simulations. To render our numerical model comparable to the analytical benchmark results derived in Section 3.2, we neglect the temperature-dependence of the ice rheology and thermal conductivity for all computations in this section.

It is unreasonable to expect that the numerical and analytical solutions match exactly, for two reasons: First, the analytical solution is an exact asymptotic result, except that its coefficient J_{tip} is known only in the limit of very wide ice streams. We therefore expect that the error between analytical and numerical results decreases with increasing ice-stream width. Second, the analytical treatment only captures the contribution to shear heating that results from the stress singularity at the bed. The effect of the nonsingular, but still intense, shear heating throughout the entire depth extent of the ice is not accounted for by the singular term only. The numerically-estimated shear heating should thus approach the analytically-estimated shear heating only in the immediate vicinity of the singularity ($r \to 0$) apart from uncertainties in the multiplying factor J_{tip}, but will deviate at non-negligible distances to the singularity. In addition to serving as a benchmark, the comparison between analytical and numerical results can hence shed light on the relative importance of shear heating in the near-field as opposed to the far-field.

Figure 5 shows an example computation for Dragon margin ($W = 34\,H$) for zero basal stress to facilitate the comparison with the analytical results, where we compare the angular dependence of dissipation defined as $2\tau_E\dot{\epsilon}_E \times r$ instead of the singular dissipation $2\tau_E\dot{\epsilon}_E$. The numerically-computed dissipation approaches the analytical value for radii on the order of a few meters. The importance of terms beyond the dominant singularity is strikingly apparent beyond 60 m from the tip, where the ordering of the angular dependence is reversed. The errors in the vicinity of the singularity is between 6-17% depending on the angle. The slight but systematic deviations at small radii in Fig. 5 are due to the analytical results requiring very wide ice streams ($W \gg H$), which is only approximately true for Dragon margin. We achieved considerably better accuracy for wider ice streams, with errors dropping to 1%.

We conclude that our simulations reproduce the magnitude of shear heating in the immediate vicinity of the singularity accurately. As the radius approaches zero, however, the numerical solutions become increasingly dominated by numerical error associated with the quickly diverging stresses and are less unreliable. The radius below which the numerical solutions become inaccurate depends primarily on the resolution. It is thus possible to resolve the singularity better than in Figure 5. Ultimately, however, there will always be a critical radius below which the analytical result is more accurate. Beyond serving as a benchmark, Figure 5 also demonstrates that the far-field contribution to shear heating becomes increasingly important at radial distances beyond a few meters, rendering the analytical solution that only captures heating in the near-field of the singularity less adequate.

4.2. The importance of a temperature-dependent rheology

The most significant assumption in analytical models of ice-stream dynamics is probably the usage of a simplified rheology, such as a constant Newtonian viscosity [*Schoof*, 2004, 2012] or a temperature-independent power-law rheology. In this section, we quantify the ramifications of using a simplified rheology by comparing our model predictions to the surface velocities at Dragon margin observed by *Echelmeyer and Harrison* [1999]. All computations in this section are based on the reduced thermal model

$$\frac{\partial}{\partial y}\left(k\frac{\partial T}{\partial y}\right) + \frac{\partial}{\partial z}\left(k\frac{\partial T}{\partial z}\right) + [1 - H(T - T_m)]\,2\tau_E\dot{\epsilon}_E = 0\,, \tag{20}$$

which neglects the advective terms and the effect of surface crevassing as compared to the full thermal model defined in Sec. 2.3. The latter two effects are discussed in detail in the subsequent sections.

In Figure 7, we compare the temperate zones and predicted surface velocities for three different rheologies. The computation on top (Figures 7A1 and B1) is based on a

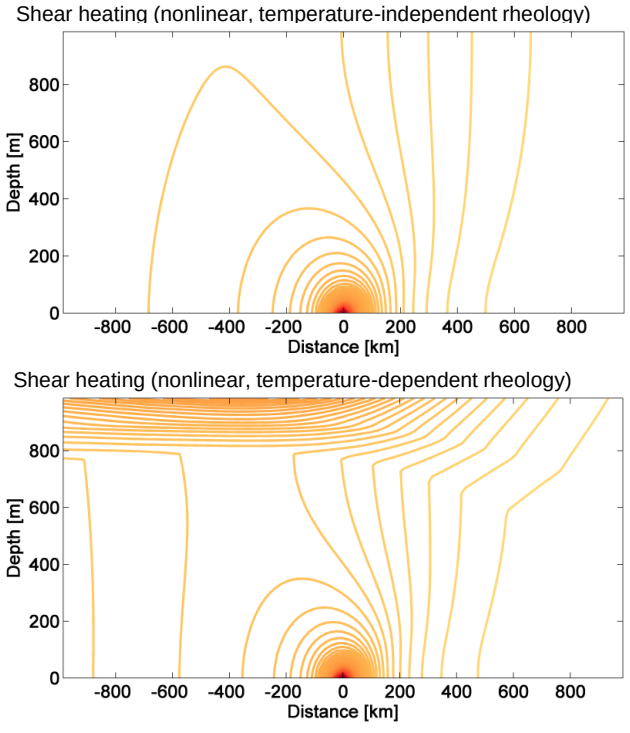

Figure 6. Eighty contours of constant shear heating in units of [Pa/yr] in the vicinity of the singularity when neglecting (top) and including (bottom) the temperature-dependence of the rheology.

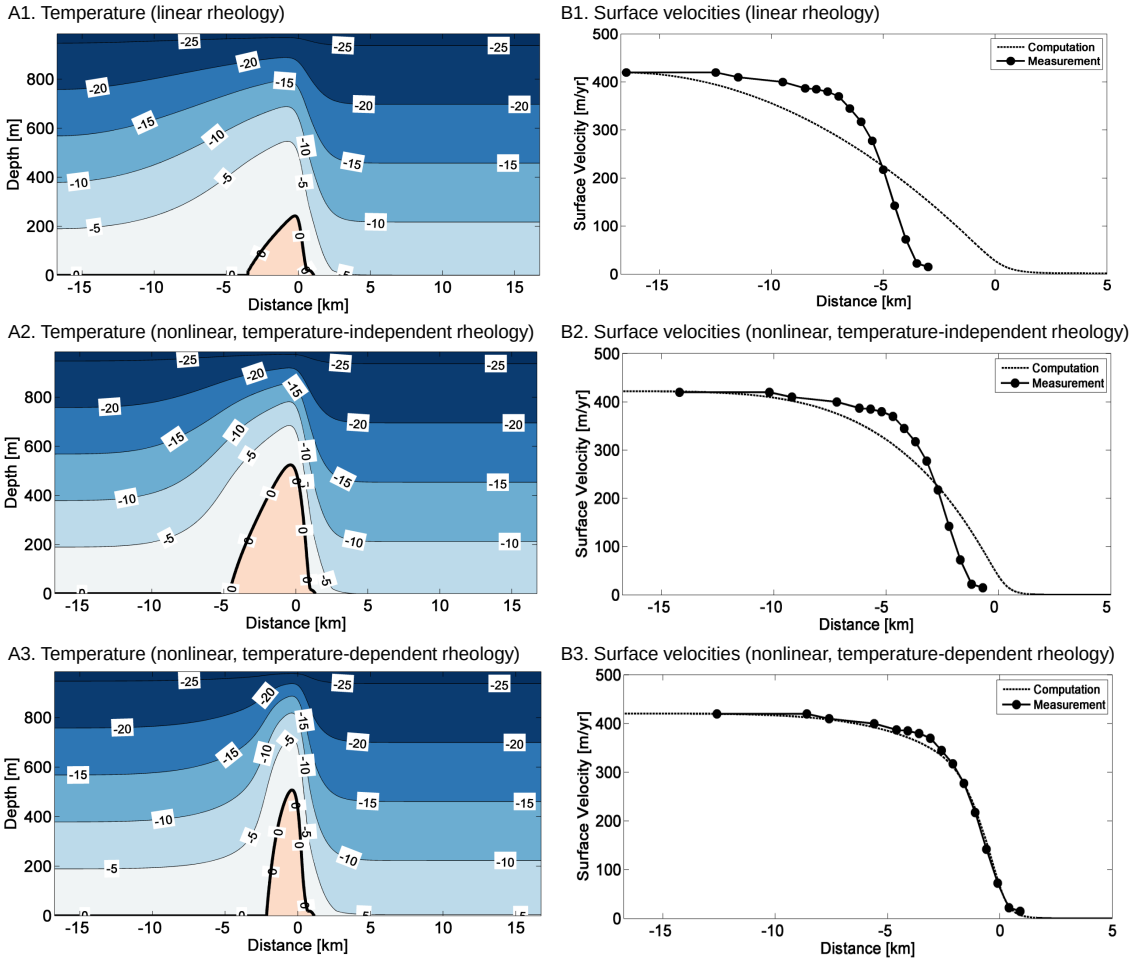

Figure 7. Top: Temperature field (A1) and surface velocities (B1) assuming a Newtonian rheology of $\mu = 10^{14}$ Pa s. Middle: Temperature field (A2) and surface velocities (B2) for a power-law rheology that accounts for the strain-rate dependence of the effective viscosity, but neglects the temperature dependence. Bottom: Temperature field (A2) and surface velocities (B2) for a realistic rheology that captures both strain-rate and temperature dependence. The best fitting basal stresses are $\tau_{base} = 2.56$ kPa (A1, B1), $\tau_{base} = 1.12$ kPa (A2, B2) and $\tau_{base} = 4.07$ kPa (A3,B3), respectively. All computations neglect advection and surface crevassing. Measured surface velocities from *Echelmeyer and Harrison* [1999].

constant Newtonian rheology of $\mu = 10^{14}$ Pa s, which clearly gives the worst fit to observational data. The computation in the middle (Figures 7A2 and B2) takes the strain-rate dependence of the rheology into account, but neglects the temperature dependence. While this scenario is clearly more realistic than the Newtonian case, the width of the shear margin is overestimated by approximately a factor of two. Considering a realistic rheology that takes both the strain-rate and the temperature dependence into account improves the fit to observations dramatically (Figures 7A3 and B3). The extent of the temperate zone in the last computation (Figures 7A3 and B3) is roughly comparable to the observations by *Clarke et al.* [2000].

Figure 6 demonstrates why the temperature dependence of the ice rheology is such an important effect. It shows the spatial variation in shear heating in the vicinity of the slip singularity for the strain-rate dependent rheologies (Figures 7A2, B2 and A3, B3). Both cases show a pronounced peak in shear heating at the slip singularity. When taking temperature into account, we find a second local maximum in shear heating at the ice surface above the singularity. The reason is that the ice is coldest on the surface, which translates into higher effective viscosity and higher shear heating than in the ice below.

We conclude that the width of the high-strain region at the margin is controlled primarily by differences in the temperature of ice and thereby in its effective viscosity. To reproduce the rapid increase in surface speeds observed at Dragon margin [*Echelmeyer and Harrison*, 1999], the ice in the margin has to be significantly warmer and thus weaker than the ice outside.

4.3. The effect of advection

The computations in Figure 7 indicate that a significant portion of the ice in Dragon margin is temperate. However, both models may overestimate the volume of temperate ice, because they do not consider the effect of cold ice being advected into the margin both from the surface and from the ridge. To better isolate the effect of horizontal as opposed to vertical advection, we study them through separate simulations. The specific forms of the thermal model we consider in this section are therefore

$$\frac{\partial}{\partial y}\left(k\frac{\partial T}{\partial y}\right)+\frac{\partial}{\partial z}\left(k\frac{\partial T}{\partial z}\right)+\rho c w\frac{\partial T}{\partial z}+ [1-H(T-T_m)]\,2\tau_E\dot{\epsilon}_E=0\,, \qquad (21)$$

and

$$\frac{\partial}{\partial y}\left(k\frac{\partial T}{\partial y}\right)+\frac{\partial}{\partial z}\left(k\frac{\partial T}{\partial z}\right)+\rho cv\frac{\partial T}{\partial y}+ [1-H(T-T_m)]\,2\tau_E\dot{\epsilon}_E=0\,, \qquad (22)$$

where v and w are the horizontal and the vertical advection velocities as defined in Sec. 2.3.

To test the effect of vertical advection only, we first assume the same basal stress ($\tau_{base} = 4.07\,\mathrm{kPa}$) as in Figure 7A3,B3 and add vertical advection based on an accumulation of $a = 0.1\,\mathrm{m/yr}$. We find that the temperate zone vanishes almost entirely. The associated surface velocities in the ice stream, however, are now much lower than observations suggest [*Echelmeyer and Harrison*, 1999]. The reason is that by cooling the margin, vertical advection makes the margin stronger and a strong margin provides more resistance against gravity. To reproduce the observed surface velocities, we have to lower the assumed basal stress underneath the ice stream to $\tau_{base} \approx 3.17\,\mathrm{kPa}$. Figures 9A1 and B1, show the resulting temperature field and surface velocities. Interestingly, the extent of the temperate zone is now comparable to Figure 7A3,B3. We thus conclude that the main effect of vertical advection, if we insist that the surface deformation data be matched, is to slightly shift the force balance between the resistance to flow provided by the shear margin as compared to basal friction. The extent of the temperate zone in the margin changes only slightly after accounting for the different basal stress required to balance gravity.

Observations suggest that Dragon margin is currently migrating outwards with a constant speed of $-7.3\,\mathrm{m/yr}$ [*Harrison et al.*, 1998], possibly more [*Echelmeyer and Harrison*, 1999]. The effect of including horizontal advection at $-7.3\,\mathrm{m/yr}$ is shown in Figures 9A2 and B2. As a consequence of the lateral influx of cold ice from the ridge, the temperate zone vanishes entirely and it becomes impossible to reproduce the rapid increase in the observed surface speed of ice in our computations. The finding that horizontal advection on the order of m/yr precludes the formation of a temperate zone is consistent with the previous study by *Jacobson and Raymond* [1998]. Our simulations indicate that horizontal advection with speeds on the order of $0.1\,\mathrm{m/yr}$ are associated with finite temperate zones, albeit smaller ones than in the absence of horizontal influx of cold ice.

Our inability to reproduce observed surface velocities for the estimated migration speeds is clearly an important caveat. We argue that the main problem is that our simplified representation of horizontal advection does not adequately represent the physics of margin migration. Two concerns in particular come to mind: First, it is highly questionable that margin migration as rapid as several m/yr can be treated through a steady-state model. Indeed, the evidence in favor of migration of Dragon margin comes primarily from surface lineations and subsurface diffractors that indicate a complex deformational history [*Clarke et al.*, 2000; *Echelmeyer and Harrison*, 1999; *Harrison et al.*, 1998] and both inward and outward migration of the margin [*Clarke et al.*, 2000]. The observational evidence thus suggest that the system has not reached a steady state. Second, Dragon margin is located close to the confluence between ice streams B1 and B2. The interaction between the two streams and the interjacent Unicorn ridge may be an important factor to consider in modeling the evolution of the system. An example for observational evidence that supports a non-trivial geometric connection between ice stream B1 and B2 is a hook-shaped surface lineation called fishhook, which connects the two streams and correlates with several near-surface strain features [*Clarke et al.*, 2000].

Nonetheless, the simulations including horizontal advection lend additional support to our previous conclusion that Dragon margin is at least partially temperate. Our computations show that only temperate ice is weak enough to concentrate strain to the degree necessary for the surface speed to increase from approximately zero to its maximum value over as little as 8 km. Cold ice as predicted in Figure 9A2,B2 is more rigid than temperate ice and consequently associated with a much wider margin than observed. The finding that Dragon margin is likely temperate at depth is consistent with *Perol and Rice* [2011]. Albeit not including horizontal advection, they predicted temperate zones in the shear margins of the active Siple-Coast ice streams using a 1D heat-transfer model in conjunction with the shear-strain rates measured by *Joughin et al.* [2002] to constrain shear heating. In fact, the size of the temperate zone estimate here for Dragon margin and the results by Perol and Rice match moderately well (Fig. 8).

4.4. The ramifications of surface crevassing

The ice streams of West Antarctica were first identified by radar detection of their crevassed margins [*Rose*, 1979], which highlights that intense surface crevassing is a characteristic feature of the Ross Ice Streams. This observation raises the question how surface crevasses affect the thermomechanics of ice-stream margins. Within the framework of our model, surface crevassing has two competing effects: On the one hand, crevasses lower the creep resistance of the ice, because of the void space they introduce into the ice. We refer to this effect as mechanical weakening. On the other hand, crevasses lower the temperature in the ice through cool winter air pooling in the crevasses [*Harrison et al.*, 1998] thus increasing the creep resistance. We call this effect thermal strengthening.

There are multiple sets of crevassing parameters that yield a comparably good fit to surface velocities. This ambiguity results primarily from the uncertainty in the mechanical-weakening factor, but also from varying the exact location of the crevassed zone and the basal shear stress. While we are able to reproduce the velocity data for Dragon margin [*Echelmeyer and Harrison*, 1999] with a wide range of modeling parameters, compatibility with temperature measurements [*Harrison et al.*, 1998] poses more constraints. Figures 12 and 10 illustrate a computation which attempts to match both data sets simultaneously. To facilitate the comparison with our simulations, we briefly summarize four key observations by *Harrison et al.* [1998]. First, the temperature for the two boreholes in the ridge, named 'OutB'

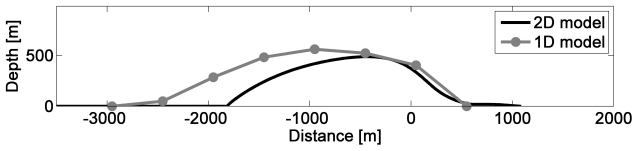

Figure 8. Comparison of the temperate zone from Fig. 9A1 and B1, replotted on a 1:1 scale, with the simplified 1D model by *Perol and Rice* [2011] using measured surface velocities *Echelmeyer and Harrison* [1999] with a surface accumulation of $a = 0.1\,\mathrm{m/yr}$ in both cases.

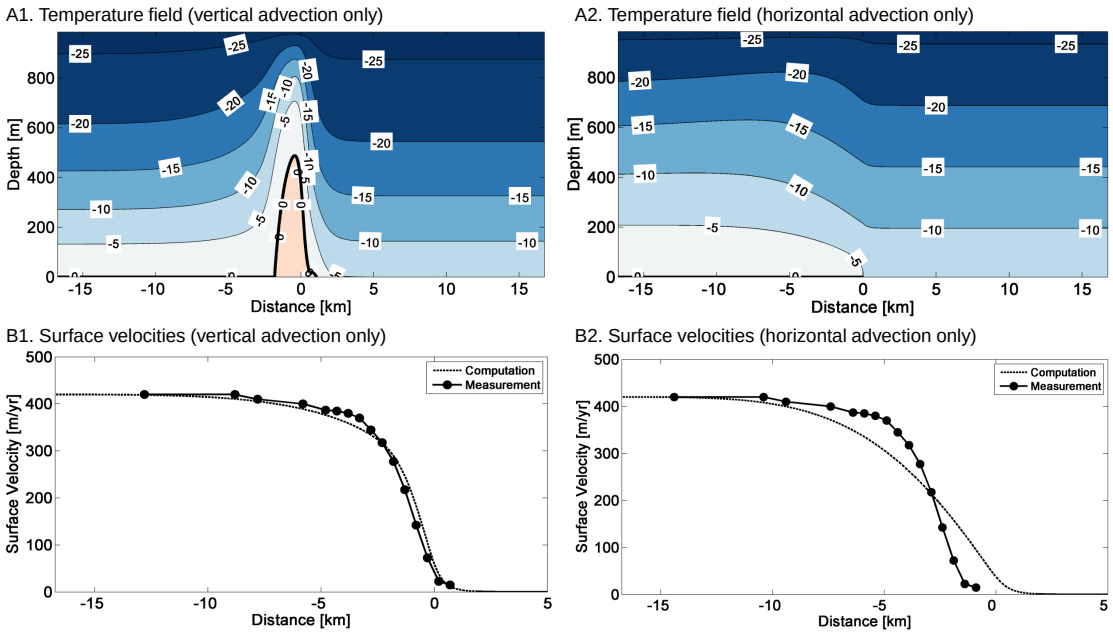

Figure 9. Temperature fields and surface velocities for Dragon margin when including only vertical advection (A1 and B1) with $a = 0.1\,\mathrm{m/yr}$ and only horizontal advection (A2 and B2) with $v = -7.3\,\mathrm{km/yr}$, respectively. The best fitting basal stresses are $\tau_{base} = 5.31\,\mathrm{kPa}$ (A1 and B1) and $\tau_{base} = 0.94\,\mathrm{kPa}$ (A2 and B2), respectively. Both computations neglect surface crevassing.

and 'Stage' (see Fig. 1 for approximate borehole locations), is approximately constant at -26°C over the depth range measured (Fig. 12). Second, out of the nine boreholes, the boreholes 'Remote', 'Intermediate' and 'Pad' exhibit the warmest temperature at depth (-22°C at a depth of approximately 700 m) with 'Intermediate' being slightly cooler than the other two. Third, borehole 'UpB', located well into the stream, is slightly cooler yet (-25°C at a depth of approximately 700 m, see Fig. 12). Fourth, the -26°C contour extends from borehole 'Dragon Pad' to borehole 'Intermediate' and attains the largest depths ($\approx 830\,\mathrm{m}$) at boreholes 'Lost Love' and 'Chaos' (Fig. 10).

Supposing that the temperatures measured by *Harrison et al.* [1998] resemble a steady state, these four observations translate into the following constraints for our modeling. First, the finding that the boreholes in the ridge maintain a typical surface temperature of -26°C over a 300 m depth interval suggests high rates of vertical advection. High vertical advection in turn implies high accumulations on the order of $a = 0.20$-$0.24\,\mathrm{m/yr}$, which may be reasonable for Antarctica. Second, the relatively warm temperatures measured for 'Remote', 'Intermediate' and 'Pad' points to internal heating at these locations. The offset between the locations of highest strain rate and highest internal heating may indicate horizontal advection probably relating to margin migration [*Echelmeyer and Harrison*, 1999; *Harrison et al.*, 1998]. Third, the comparatively cooler temperatures at 'UpB' are consistent with a localized heat source close to 'Remote', 'Intermediate', and 'Pad' that does not extend far into the stream. Fourth, we take the -26°C contour as a proxy for the extent and location of the crevassed zone at Dragon margin, which stretches from 'Dragon Pad' to 'Intermediate'.

Figure 12A shows the computed temperatures in our modeling domain. The cooling effect of crevassing depresses the temperature notably in the vicinity of the shear margin. We also compare computed and measured temperatures at a depth of 700 m for the three boreholes that are located far from the margin. The temperatures we estimate are 1-2° higher than the measured values. The fit to surface velocities (Fig. 12B) is slightly less satisfactory than in previous simulations (e.g. Fig. 7B3 and Fig. 9B1). While it is certainly possible to improve the fit to surface velocities, doing so comes at the cost of deteriorating the fit to the available temperature data.

Figure 10 compares the computed and measured temperatures for the boreholes in the vicinity of the shear margin at a depth of 700 m for the same computation also shown in Figure 12. We successfully reproduce the extent and approximate depths of the -26°C contour from *Harrison et al.* [1998], highlighted on the boreholes 'Dragon Pad' to 'Intermediate' as short horizontal dashes. Our computations are also consistent with the observation that the three leftmost boreholes are warmest and that the borehole 'Intermediate' is colder than its two neighboring boreholes. We suggest that the relatively warmer temperatures at these three boreholes could result from their proximity to a temperate zone instead of non-steady state affects as argued in *Harrison et al.* [1998]. Despite being able to reproduces these key features, the temperatures we compute are systematically too high by 1-6°C with the highest errors occurring at the boreholes closest to the margin (i.e. 'Dragon Pad', 'Lost Love' and 'Chaos').

Figure 11 summarizes the relationship between the average absolute errors in reproducing the observational data and the properties of the temperate zones for various speeds of horizontal advection v_0. The speed of horizontal advection is the most consequential parameter when reproducing both data sets simultaneously, because it has a strong effect on the temperatures and dynamics of the shear margin. The

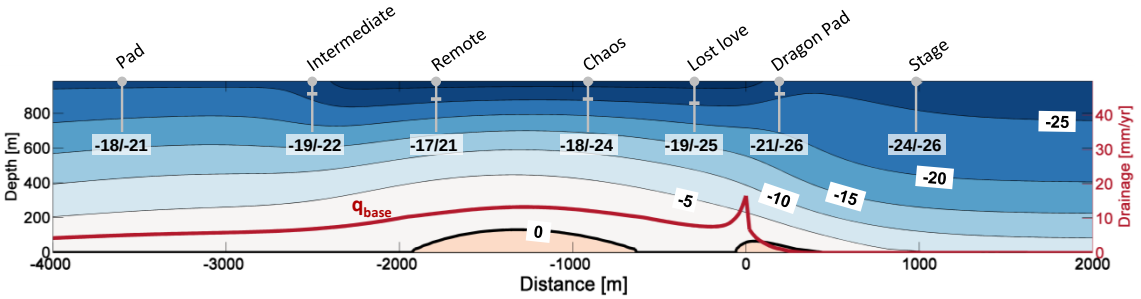

Figure 10. Extent of a potential temperate zone at Dragon margin plotted on a 1:1 scale and meltwater flux at the base of the ice, q_{base}, in mm/yr (grey line) for the computation also shown in Fig. 12. The total meltwater produced in the temperate zone is $25\,\mathrm{m}^2/\mathrm{yr}$. The approximate locations of the boreholes from *Harrison et al.* [1998] are highlighted in grey with the left number representing the computed temperature and the right value the measured temperature at a depth of approximately 700 m. Small horizontal dashes along the boreholes in the vicinity of the shear margin indicate the approximate position of the $-26°\mathrm{C}$ contour.

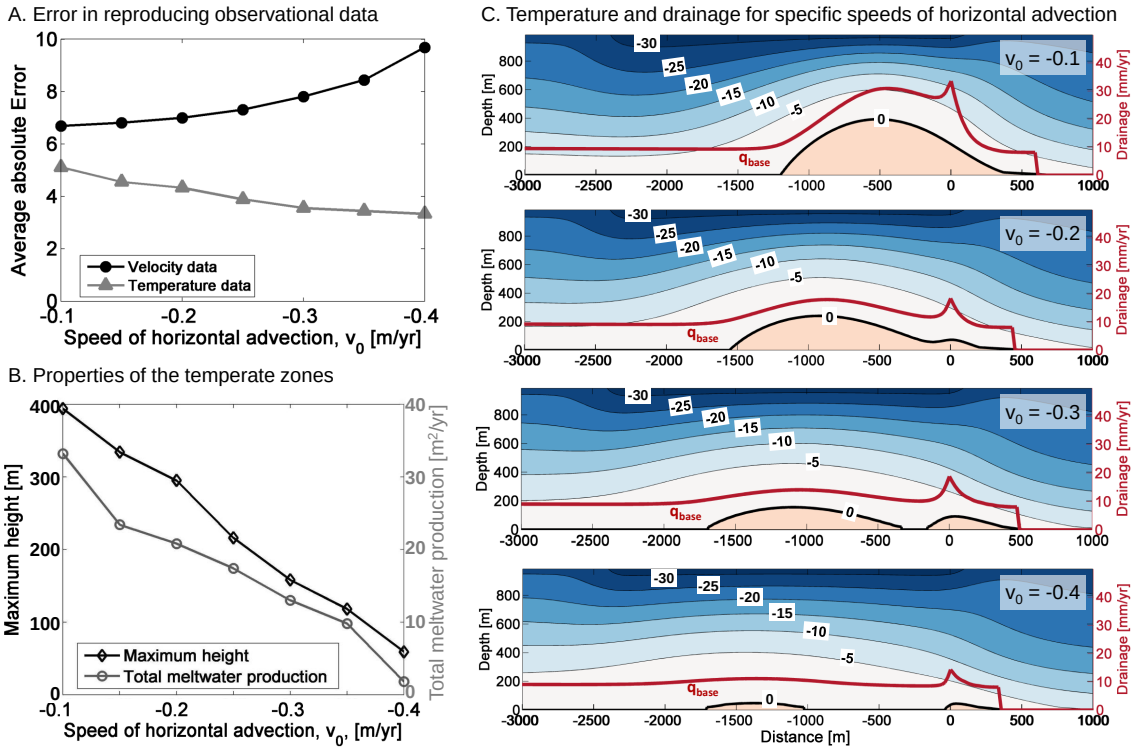

Figure 11. A. Average absolute error in reproducing observed temperatures and velocities for horizontal advection speeds between $v_0 = -0.1$ and $-0.4\,\mathrm{m/yr}$. B. Maximum height of the temperate zones and total meltwater production for horizontal advection speeds between -0.1 and $-0.4\,\mathrm{m/yr}$. The total meltwater production is computed by integrating the basal meltwater flux, q_{base} over the width of the zone where ice is temperate not only at the bed but at finite depth. C. Temperature fields and drainage curves for the four horizontal advection speeds $v_0 = -0.1, -0.2, -0.3$ and $-0.4\,\mathrm{m/yr}$, respectively. From top to bottom, the best-fitting basal stresses are $\tau_{base} = 1.57, 1.44, 1.31$ and $1.13\,\mathrm{kPa}$. Apart from the speed of horizontal advection and basal stress, all computations are based on the same model parameters, most importantly $a = 0.23\,\mathrm{m/yr}$ and $G = 85\,\mathrm{mW/m}^2$.

speed of vertical advection, on the other hand, is reasonably well constrained by fitting the temperature measurements in boreholes 'OutB' and 'Stage' (Fig. 12A) and does not af-

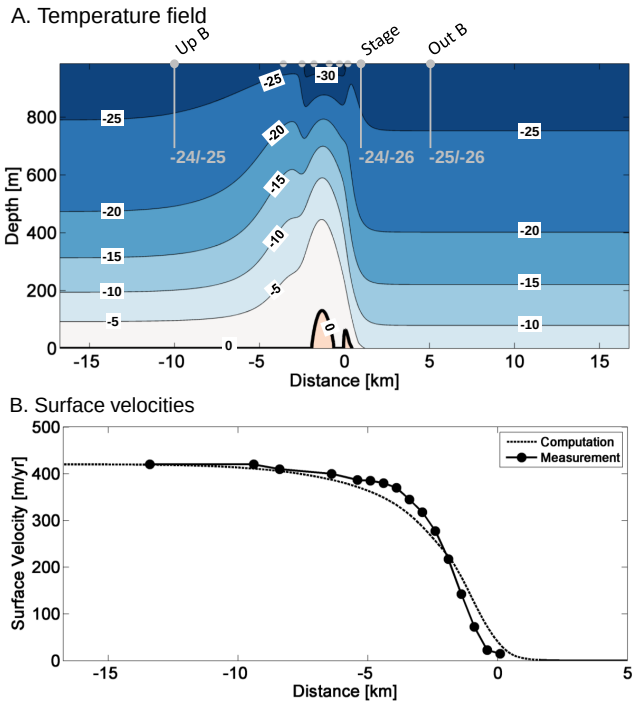

Figure 12. Temperature field (A) and surface velocities (B) for Dragon when attempting to match the observed borehole temperatures [*Harrison et al.*, 1998], see Figs. 1 and 2 for borehole locations, and surface velocities [*Echelmeyer and Harrison*, 1999] simultaneously. The computation is based on the model parameters $\tau_{base} = 1.22\,\mathrm{kPa}$, accumulation $a = 0.23\,\mathrm{m/yr}$, geothermal heat flux $G = 85\,\mathrm{mW/m^2}$, and horizontal advection at $v = -0.35\,\mathrm{m/yr}$. The approximate locations of the nine boreholes considered in *Harrison et al.* [1998] are indicated as grey dots. We highlight the boreholes located far from margin as grey lines in accordance to their depth. The left numbers represent the computed value and the right number the measured value at maximum depth. The corresponding temperature estimates for the boreholes in the vicinity of the margin are shown in the next figure.

fect the shear margin as sensitively (see also the discussion in Sec. 4.3). Figure 11 highlights that the maximum height and the shape of the temperate zones are highly dependent on the assumed speed of horizontal advection and that large temperate zones tend to produce a better fit to the observed velocities while small temperate zones produce more realistic temperatures. We argue that horizontal-advection speeds on the order of $v_0 = -0.3$ to $-0.35\,\mathrm{m/yr}$ probably provide a reasonable compromise (Figs. 12 and 10 show the case where $v_0 = -0.35\,\mathrm{m/yr}$). Increasing the speed of horizontal advection beyond $v_0 \approx -0.35\,\mathrm{m/yr}$ deteriorates the fit to observed surface velocities notably (similar to Fig. 9B2) while improving the match to measured temperatures only minimally.

The temperate zones for horizontal-advection speeds between $v_0 = -0.3$ and $-0.35\,\mathrm{m/yr}$ reach a maximum height of 120-160 m. In the vicinity of the locked-to-sliding transition point, the height of the temperate zone has a second maximum of approximately 80 m. The width of the temperate zones, which we define as the maximum width range over which ice is temperate not only at the bed but at a finite depth, are approximately 2.2 and 2.3 km. We obtain the total meltwater production by integrating the basal meltwater flux over the temperate zone, which extends from about $y = -16.94\,\mathrm{km}$ to $y = 512\,\mathrm{m}$ for $v_0 = -0.30\,\mathrm{m/yr}$ and from $y = -19.30\,\mathrm{km}$ to $y = 413\,\mathrm{m}$ for $v_0 = -0.35\,\mathrm{m/yr}$, is 26.5 and $25\,\mathrm{m^3/yr}$ and meter in downstream direction, respectively. Increasing the rate of outward margin migration, shifts the temperate zone further into the stream, depresses the maximum depth to which temperate ice extends and decreases the total meltwater production (Fig. 11).

When weighing how to prioritize the two data sets, it is important to keep in mind that a steady-state approach to modelling the temperatures throughout Dragon margin is in itself highly questionable (see also Sec. 4.3). A simple scaling analysis shows that the time it takes for the full ice thickness to reach steady state, $t = H^2/\alpha_{th}$, is approximately 10^4 years. In contrast, *Harrison et al.* [1998] estimated the residence time of ice in Dragon margin is approximately a half century. It is thus clear that the stream-ridge system can not possibly be in steady state. This insight is supported by field observations that indicate a complex deformational history dating back over the last few hundred years [*Clarke et al.*, 2000; *Echelmeyer and Harrison*, 1999; *Harrison et al.*, 1998]. Non-steady state effects should be most significant for the boreholes closest to the margin, because of the rapid margin migration in recent years [*Echelmeyer and Harrison*, 1999; *Harrison et al.*, 1998]. The observation that the deviations between computed and observed temperatures are indeed highest in the shear margin lends support to the interpretation that non-steady effects are probably the main reason for the temperature mismatch between model and data.

5. Discussion

While several previous models of ice streams [*Perol and Rice*, 2011; *Schoof*, 2004; *Jacobson and Raymond*, 1998] have raised the possibility of melting in active ice-stream margins, only *Perol and Rice* [2011] discuss the extent of a potential temperate zone in detail (see Figure 8 for a comparison with their results). Our goal in this study is to provide additional constraints on how different factors such as a strong stress concentration at the bed modeled as a singularity (Sec. 4.1), the assumed ice rheology (Sec. 4.2), horizontal and vertical advection (Sec. 4.3) and surface crevassing (Sec. 4.4) affect deformation-induced melting and the size of the temperate zone, if any.

A model that strives to represent ice-stream margins in a somewhat realistic way inevitably entails a large number of parameters. In our case, the majority of model parameters relate to the ice rheology. To limit the ambiguity introduced into our model by a large number of parameters, we decided not to vary the rheological parameters. As detailed in Sec. 2, we adopt the recommended parameter values in *Cuffey and Paterson* [2010] and an enhancement factor of $E = 1$. When neglecting surface crevassing, our model is thus reduced to one free variable, the basal shear stress underneath the stream. Incorporating surface crevassing requires new model parameters, but varying the extent of the crevassed zone has little effect on our results within the parameter ranges consistent with observations (Sec. 2.5).

Throughout this paper, we focus primarily on reproducing the surface velocities observed by [*Echelmeyer and Harrison*, 1999]. The simulations including surface crevassing (Sec. 4.4), however, also lend themselves to a comparison with the temperature data by [*Harrison et al.*, 1998]. Consistency with the temperature data requires high rates of

vertical and horizontal advection (Sec. 4.4). A perfect fit to the observed temperatures can not be expected within the confines of a steady-state model (see Sec. 4.4), particularly for a location with a complex deformational history like Dragon margin [*Clarke et al.*, 2000]. We therefore argue that the computation shown in Figs. 12 and 10 represents a reasonable compromise between the velocity [*Echelmeyer and Harrison*, 1999] and the temperature [*Harrison et al.*, 1998] data. This particular computation entails a temperate zone with a maximum height of $\approx 120\,\mathrm{m}$ and entails a meltwater production of $25\,\mathrm{m}^3/\mathrm{yr}$ per meter in downstream direction (Fig. 10).

In two previous studies, *Echelmeyer et al.* [1994] and *Scambos et al.* [1994] have chosen to adjust the enhancement factor and its spatial variability in the model domain to reproduce the observed surface velocities computationally. It is certainly possible to match the surface velocity *Echelmeyer and Harrison* [1999] and temperature [*Harrison et al.*, 1998] data for Dragon margin only by varying enhancement in different parts of the stream-ridge system. However, we require very high enhancement values on the order of 15-20 in the shear margin to obtain a satisfactory fit to observational data, which conflicts with the results of *Jackson and Kamb* [1997] who determined enhancement factors between $E \approx 1.12$ and $E \approx 2.55$ for different ice specimen retrieved from Dragon margin.

Our simulations show that it is not necessary to resort to very high enhancement factors to reproduce rapid velocity increases in shear margins. We obtain excellent fits to surface velocities even when neglecting enhancement entirely. This insight is not meant to imply that varied effects such as fabric, impurities or grain-size variations, which are usually integrated into a single enhancement factor, are not important. Instead, we argue that the relatively small enhancement factors measured at Dragon margin [*Jackson and Kamb*, 1997] in combination with our simulations suggest that enhancement effects are probably not the whole story and that deformation-induced melting may play an important role in the thermomechanics of ice-stream margins as well. As commented by *Perol and Rice* [2013], two pieces of observational evidence lend additional support to this possbility: *Clarke et al.* [2000] mapped a prominent diffractor under Unicorn ridge that may indicate a former temperate zone, and drilling into a now inactive margin by *Vogel et al.* [2005] revealed flowing water in a 1.6 m deep gap between the base of the ice sheet and the till below.

6. Conclusion

The goal of this study is to investigate the possibility of deformation-induced melting in active shear margins. Melting and the associated presence of meltwater in ice-stream margins might have important consequences for the dynamics of ice streams, primarily because the yield strength of glacial till depends sensitively on porosity, which is controlled by the water content if saturated. The position of the shear margins could thus be intricately linked to meltwater production, which remains poorly constrained. We devise a 2D thermomechanical model of an ice stream moving over a plastic bed in steady state. We solve our model numerically after carefully benchmarking our computational approach against an asymptotic analytic solution. In combination with previous studies [*Perol and Rice*, 2013; *Schoof*, 2004; *Jacobson and Raymond*, 1998], our simulations lend theoretical support to the hypothesis that active shear margins are partially temperate. For Dragon margin, we estimate a temperate zone with a maximum height of ~ 120 to 150 m that produces approximately 25 to $26.5\,\mathrm{m}^3/\mathrm{yr}$ of meltwater per meter in downstream direction. This estimate for the extent of a temperate zone is roughly comparable to the height of the bottom diffractor identified by *Clarke et al.* [2000] under Unicorn Ridge. Despite focusing primarily on Dragon margin, we argue that our insights may generalize to the other active Ross Ice Streams.

Acknowledgments. This research was supported by the National Science Foundation through Office of Polar Programs grant ANT-0739444, the Geomechanics Research Fund and the Center for the Environment at Harvard University. The authors thank Richard Alley, Garry Clarke, Timothy Creyts, Ian Hewitt, Ian Joughin, and Christian Schoof for fruitful discussions.

References

Alley, R., D. Blankenship, C. Bentley, and S. Rooney, Deformation of till beneath Ice Stream B, West Antarctica, *Nature*, *322*, 57–59, 1986.

Bamber, J. L., D. G. Vaughan, and I. Joughin, Widespread complex flow in the interior of the antarctic ice sheet, *Science*, *287*(5456), 1248–1250, 2000.

Beem, L., K. Jezek, and C. Van der Veen, Basal melt rates beneath Whillans Ice Stream, West Antarctica, *Journal of Glaciology*, *56*(198), 647–654, 2010.

Ben Amar, M., and J. Rice, Exacts results with the J-integral applied to free-boundary flows, *Journal of Fluid Mechanics*, *461*, 321–341, 2002.

Bilby, B., and J. Eshelby, Dislocations and the Theory of Fracture, in *Fracture: An Advanced Treatise: Vol. 2, Mathematical Fundamentals*, edited by H. Liebowitz, pp. 99–182, Academic Press, N.Y., 1968.

Bindschadler, R., and P. Vornberger, Changes in the west antarctic ice sheet since 1963 from declassified satellite photography, *Science*, *279*(5351), 689–692, 1998.

Briggs, W. L., V. E. Henson, and S. F. McCormick, *A Multigrid Tutorial*, vol. 72, Siam Monograph, 2000.

Cherepanov, G., Cracks in solids, *International Journal of Solids and Structures*, *4*(8), 811–831, 1968.

Clarke, T. S., C. Liu, N. E. Lord, and C. R. Bentley, Evidence for a recently abandoned shear margin adjacent to ice stream B2, Antarctica, from ice-penetrating radar measurements, *Journal of Geophysical Research*, *105*(B6), 2000.

Cuffey, K., and W. Paterson, *The Physics of Glaciers (Fourth Edition)*, ISBN 9780123694614, Elsevier, 2010.

Dreimanis, A., *Genetic classification of glacigenic deposits*, chap. Tills: their genetic terminology and classification, pp. 17–83, Balkema, Rotterdam, 1988.

Echelmeyer, K., and W. Harrison, Ongoing margin migration of ice stream b, antarctica, *Journal of Glaciology*, *45*(150), 361–369, 1999.

Echelmeyer, K., W. Harrison, C. Larsen, and J. Mitchell, The role of the margins in the dynamics of an active ice stream, *Journal of Glaciology*, *40*(136), 527–538, 1994.

Engelhardt, H., N. Humphrey, B. Kamb, and M. Fahnestock, Physical conditions at the base of a fast moving antarctic ice stream, *Science*, *248*, 57–59, 1990.

Fahnestock, M., T. Scambos, R. Bindschadler, and G. Kvaran, A millennium of variable ice flow recorded by the ross ice shelf, antarctica, *J. Glaciol.*, *46*(155), 652–664, 2000.

Frost, H., and M. Ashby, Deformation mechanism maps: the plasticity and creep of metals and ceramics, 1982.

Goldman, N. L., and J. W. Hutchinson, Fully plastic crack problems: The center-cracked strip under plane strain, *International Journal of Solids and Structures*, *11*(5), 575–591, 1975.

Harrison, W., K. A. Echelmeyer, and C. Larsen, Measurement of temperature in a margin of Ice Stream B, Antarctica : implications for margin migration and lateral drag, *Journal of Glaciology*, *44*(148), 1998.

Iverson, N., T. Hooyer, and R. Baker, Ring-shear studies of till deforrnation: Coulotnb-plastic behavior and distributed strain in glacier beds, *Journal of Glaciology*, *44*(148), 634–642, 1998.

Jackson, M., and B. Kamb, The marginal shear stress of Ice Stream B, West Antarctica, *Journal of Glaciology*, *43*(145), 415–426, 1997.

Jacobel, R., T. Scambos, C. Raymond, and A. Gades, Changes in the configuration of ice stream flow from the west antarctic ice sheet, *Journal of Geophysical Research*, *101*(B3), 5499–5504, 1996.

Jacobel, R., T. Scambos, N. Nereson, and C. Raymond, Changes in the margin of ice stream c, antarctica, *Journal of Glaciology*, *46*(152), 102–110, 2000.

Jacobson, H., and C. Raymond, Thermal effects on the location of ice stream margins, *Journal of Geophysical Research*, *103*(B6), 111–122, 1998.

Jordan, R., and J. Stark, Capillary Tension in Rotting Ice Laters, *Tech. rep.*, Technical Report ERDC/CRREL TR-01-13. US Army Corps of Engineers, Cold Regions Research and Engineering Laboratory, 2001.

Joughin, I., S. Tulaczyk, R. Bindschadler, and S. F. Price, Changes in West Antarctic Ice Stream velocities: Observation and analysis, *Journal of Geophysical Research*, *107*(B11), doi: 10.1029/2001JB001029, 2002.

Joughin, I., D. R. MacAyeal, and S. Tulaczyk, Basal shear stress of the Ross ice streams from control method inversions, *Journal of Geophysical Research*, *109*(B9), doi: 10.1029/2003JB002960, 2004.

Kamb, B., Rheological nonlinearity and flow instability in the deforming bed mechanism of ice stream motion, *Journal of Geophysical Research*, *96*(B10), 16,58516,595, 1991.

Kamb, B., Basal zone of the West Antarctic Ice Streams and its role in lubrication of their rapid motion, in *The West Antarctic Ice Sheet: Behavior and Environment*, vol. 77, edited by R. B. Alley and R. A. Bindschadler, pp. 157–199, AGU, Washington, DC, doi:10.1029/AR077p0157, 2001.

Kubo, S., K. Ohji, and K. Ogura, Analysis of creep crack-propagation on the basis of the plastic singular stress-field, *Engineering Fracture Mechanics*, *11*(2), 315–329, 1979.

Landes, J., and J. Begley, A fracture mechanics approach to fatigue crack growth, in *Mechanics of Crack Growth*, pp. 128–148, Amer. Soc. for Testing and Materials (ASTM), Special Technical Publication (STP) 590, Philadelphia, 1976.

Lliboutry, L., Temperate ice permeability, stability of water veins and percolation of internal meltwater, *Journal of Glaciology*, *42*(141), 201–211, 1996.

McMeeking, R., and R. Johnson, On the mechanics of surging glaciers, *Journal of Glaciology*, *32*(110), 120–132, 1986.

Perol, T., and J. R. Rice, Control of the width of West Antarctic ice streams by internal melting in the ice sheet near the margins, abstract C11B-0677 presented at 2011 Fall Meeting, AGU, San Francisco, Calif., 5-9 Dec., 2011.

Perol, T., and J. R. Rice, Control on the width of active siple coast ice streams by internal melting at their margins, in revision for submission to *Journal of Geophysical Research*, 2013.

Rathbun, A., C.Marone, R. Alley, and S. Anandakrishnan, Laboratory study of the frictional rheology of sheared till, *Journal of Geophysical Research*, *113*(F02020), doi:10.1029/2007JF000815, 2008.

Rice, J., Stresses due to a sharp notch in a work hardening elastic-plastic material loaded by longitudinal shear, *Journal of Applied Mechanics*, *34*, 287–298, 1967.

Rice, J., A path independent integral and the approximate analysis of strain concentration by notches and cracks, *Journal of Applied Mechanics*, *35*, 379–386, 1968a.

Rice, J., Mathematical analysis in the mechanics of fracture, in *Fracture: An Advanced Treatise: Vol. 2, Mathematical Fundamentals*, edited by H. Liebowitz, pp. 191–311, Academic Press, N.Y., 1968b.

Rose, K., Characteristics of ice flow in Marie Byrd Land, Antarctica, *Journal of Glaciology*, *24*, 63–75, 1979.

Scambos, T., K. Echelmeyer, M. Fahnestock, and R. Bindschadler, Develoment of enhanced ice flow at the southern margin of Ice Stream D, Antarctica, *Annals of Glaciology*, *20*, 313–318, 1994.

Schofield, A., and P. Wroth, *Critical state soil mechanics*, McGraw-Hill London, 1968.

Schoof, C., On the mechanics of ice-stream shear margins, *Journal of Glaciology*, *50*(169), 208–218, 2004.

Schoof, C., Thermally driven migration of ice-stream shear margins, *Journal of Fluid Mechanics*, *1*(1), 1–28, 2012.

Shabtaie, S., and C. Bentley, West Antarctic Ice Streams Draining into the Ross Ice Shelf: Configuration and Mass Balance, *Journal of Geophysical Research*, *92*, 1311–1336, 1987.

Shabtaie, S., and C. Bentley, Ice-thickness map of the west antarctic ice streams by radar sounding, *Ann. Glaciol.*, *11*, 126–136, 1988.

Tulaczyk, S., Ice sliding over weak, fine-grained tills: dependence of ice-till interactions on till granulometry, *Geological Society of America Special Papers*, *337*, 159–177, 1999.

Tulaczyk, S., B. Kamb, R. P. Scherer, and H. F. Engelhardt, Sedimentary processes at the base of a West Antarctic ice stream; constraints from textural and compositional properties of subglacial debris, *Journal of Sedimentary Research*, *68*(3), 487–496, 1998.

Tulaczyk, S., W. B. Kamb, and H. Engelhardt, Basal mechanics of Ice Stream B, West Antarctica 1. till mechanics, *Journal of Geophysical Research*, *105*(B1), 463–481, doi: 10.1029/1999JB900329, 2000.

Vogel, S. W., S. Tulaczyk, B. Kamb, H. Engelhardt, F. D. Carsey, A. E. Behar, A. L. Lane, and I. Joughin, Subglacial conditions during and after stoppage of an Antarctic Ice Stream: Is reactivation imminent?, *Geophysical Research Letter*, *32*, doi:10.1029/2005GL022563, 2005.

Vornberger, P., and I. Whillans, Crevasse deformation and examples from ice stream b, antarctica, *Journal of Glaciology*, *36*(122), 3–10, 1990.

Whillans, I., and C. Van Der Veen, New and improved determinations of velocity of Ice Stremas B and C, West Antarctica, *Journal of Glaciology*, 1993.

Whillans, I., and C. Van der Veen, Transmission of stress between an ice stream and interstream ridge, *Journal of Glaciology*, *47*(158), 433–440, 2001.

Zotikov, I., *The Thermophysics Of Glaciers*, D. Reidel, Mass, 1986.

Appendix A: The near-tip field parametrized by J_{tip}

By reinterpreting the material rheology a parallel can be drawn between the downstream velocity profile in a two-dimensional margin and an anti-plane crack problem. In an elastic (or "deformation theory" elastic-plastic) body the stress depends on the strain, while in the viscous material considered here the stress depends on the strain rate. The stress fields in the elastic and viscous problems are identical, strain rate in the viscous problem is analogous to strain in the elastic problem, and downstream velocity is analogous to displacement.

In this section we will solve analytically for the shear heating profile near the point where the bed transitions from slipping to locking. To develop the analytic solution we must neglect the temperature dependence of the rheology and assume a relationship of the form

$$\dot{\epsilon}_E = A\tau_E^n, \tag{A1}$$

where A and n are constant. Our problem is now mathematically equivalent to the anti-plane crack problem solved in *Rice* [1967, 1968b], which solved for the stress field in a material with a linear stress-strain relationship up to a given yield stress and an arbitrary non-linear stress-strain relationship (including a power-law relationship as a special case) above the yield stress. The solution in *Rice* [1967] relies on a transformation to the hodograph plane. This transformation interchanges the dependent and independent variables, allowing us to solve for y and z as a function of the strain rate components $\dot{\epsilon}_{xz}$ and $\dot{\epsilon}_{yz}$. As shown in *Rice* [1967], the solution for the field near the crack tip takes the form

$$y = X(\dot{\epsilon}_E) + F(\dot{\epsilon}_E)\cos 2\phi \quad , \quad z = F(\dot{\epsilon}_E)\sin 2\phi \tag{A2}$$

where we have used the polar coordinates,

$$\dot{\epsilon}_{xy} = -\dot{\epsilon}_E \sin\phi \quad , \quad \dot{\epsilon}_{xz} = \dot{\epsilon}_E \cos\phi. \tag{A3}$$

For the power-law rheology given in equation (A1) the functions $X(\dot{\epsilon}_E)$ and $F(\dot{\epsilon}_E)$ are

$$F(\dot{\epsilon}_E) = \frac{J_{tip}}{2\pi\dot{\epsilon}_E\tau_E(\dot{\epsilon}_E)} \quad , \quad X(\dot{\epsilon}_E) = \frac{n-1}{n+1}F(\dot{\epsilon}_E), \tag{A4}$$

where the constant J_{tip} is determined by the far-field loading on the margin, and the evaluation of J_{tip} will be discussed in detail in Appendix B. The function $F(\dot{\epsilon}_E)$ can then be related to the shear-heating rate through

$$2\tau_E\dot{\epsilon}_E = \frac{J_{tip}}{\pi F(\dot{\epsilon}_E)}. \tag{A5}$$

To solve for $F(\dot{\epsilon}_E)$ we first eliminate ϕ from equation (A4), which uncovers the equation for a circle

$$(y - X(\dot{\epsilon}_E))^2 + z^2 = F(\dot{\epsilon}_E)^2. \tag{A6}$$

Thus, lines of constant shear heating form circles in the (y, z)-plane with a radius of $F(\dot{\epsilon}_E)$ and a center at $y = X(\dot{\epsilon}_E), z = 0$.

For a Newtonian rheology ($n = 1$), $X(\dot{\epsilon}_E) = 0$ and equation (A6) simplifies to,

$$2\tau_E\dot{\epsilon}_E = \frac{J_{tip}}{\pi r}, \tag{A7}$$

where $r = \sqrt{y^2 + z^2}$. This means that lines of constant frictional heating form circles about the point where the bed transitions from slipping to locking, and thus the shear heating within the ridge and the ice stream is the same. For the more realistic Glen's law rheology ($n = 3$) the solution is more complicated. In this case $X(\dot{\epsilon}_E) = F(\dot{\epsilon}_E)/2$, and equation (A6) is a quadratic equation in $F(\dot{\epsilon}_E)$. Noting that $F > 0$ is required for a physically relevant frictional heating profile, the only solution is

$$F(\dot{\epsilon}_E) = \frac{2}{3}\left(\sqrt{4y^2 + 3z^2} - y\right). \tag{A8}$$

This can be simplified by using polar coordinates centered on the transition point,

$$y = r\cos\theta \quad , \quad z = r\sin\theta \tag{A9}$$

leading to the final from of the frictional heating profile

$$2\tau_E\dot{\epsilon}_E = \frac{3J_{tip}}{2\pi r}\left(\sqrt{4 - \sin^2\theta} - \cos\theta\right). \tag{A10}$$

For Glen's law the circles that show the lines of constant shear heating are no longer centered on the transition point, but are shifted towards the ridge by an amount $X(\dot{\epsilon}_E) = J_{tip}/(4\pi\tau_E\dot{\epsilon}_E)$ that varies with the magnitude of shear heating. This means that the shear heating is skewed, with more intense heating in the ridge than the ice stream.

Appendix B: J-integral evaluation for an anti-plane flow

In this section we use a path independent integral to evaluate the constant J_{tip} from Appendix A, linking the far-field loading on the ice stream to the shear heating singularity near the transition from a slipping to a locking bed. This is an extension to the J-integral commonly used in fracture mechanics [*Rice*, 1968a, b; *Cherepanov*, 1968]. Path-independent integral concepts have been applied to creeping solids before, as shown in *Landes and Begley* [1976], *Kubo et al.* [1979], or *Ben Amar and Rice* [2002], and more explicitly applied to glacial flow by *McMeeking and Johnson* [1986].

Our domain of ice is made to coincide with that of a classical anti-plane crack problem, for an ice slab of thickness $2H$, when we add to our domain its mirror image about the base. Thus, we have a classical crack problem with $u = 0$ along the prolongation of the slipping zone into the locked zone $z = 0$ and $y > 0$, gravity loadings in the respective domains $z > 0$ and $z < 0$, fraction-free surfaces, $\tau_{zx} = 0$, at $z = \pm H$ and with $\tau_{zx} = \tau_{base}$ on both sides of $z = 0$ where $y < 0$.

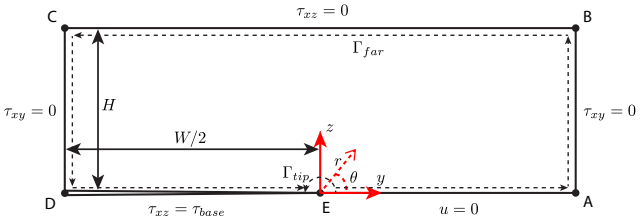

Figure 13. Sketch showing the two paths Γ_{tip} and Γ_{far} used to evaluate the path independent integral defined in eq. B1. Γ_{tip} is taken sufficiently close to the transition point that the stress field is described by the solution in Appendix A and Γ_{far} is evaluated along the border of the domain.

Assuming that the properties of ice do not change with temperature (or that temperature varies only with z), the appropriate path-independent integral for our problem is

$$J = \int_\Gamma \left(\Phi(\dot{\epsilon_E}, z) - \rho g \sin\alpha\, u\right) \mathrm{d}z - \boldsymbol{\tau} \cdot \mathbf{n} \frac{\partial u}{\partial y} \mathrm{d}s, \qquad \text{(B1)}$$

where $\boldsymbol{\tau} = (\tau_{xy}, \tau_{yz})$, Φ is analogous to the strain energy density function from elasticity and is defined for a creeping solid as

$$\Phi(\dot{\epsilon}_E) = 2\int_0^{\dot{\epsilon}_E} \tau_E\left(\xi\right) \mathrm{d}\xi\,, \qquad \text{(B2)}$$

$\mathbf{n}$ is the outward unit normal to the curve Γ, and $\mathrm{d}s$ is evaluated in a counter-clockwise fashion. For any closed curve Γ that does not enclose the transition point (i.e., the crack tip), $J = 0$ so that the is integral path-independent.

For classical crack problems, Γ is taken to start on the lower crack surface $z = 0^-$, $y < 0$, encircle the crack tip, and end on the upper crack surface $z = 0^+$, $y < 0$. J is independent of path Γ for all paths with the same starting and ending points. If there is no traction on the crack faces ($\tau_{base} = 0$), J is independent of where we start and end along the faces. When $\tau_{base} \neq 0$, we start and end at points $y < 0$ which are close to the tip, and in the limit when $y \to 0$ on both faces, we define J_{tip} as the value of J. Subsequently, we focus on the part of any path Γ in the domain $z \geq 0$ so that the result of eq. B1, taken along that part of the path, is $J_{tip}/2$.

We now evaluate J_{tip} along the two curves Γ_{tip} and Γ_{far} shown in Figure 13, which meet these specifications, with Γ_{tip} sufficiently close to the transition point that the deformation can be described by the solution in Appendix A. Evaluation along Γ_{tip} just confirms the relations involving J_{tip} in that appendix. For a typical ice stream geometry the contribution to J from the portion of Γ_{far} in the center of the ridge is negligible, so for the boundary conditions highlighted in Fig. 13

$$\frac{J_{tip}}{2} = \int_H^0 \left[\Phi\left(\dot{\epsilon}_{xz}\right) - \rho g \sin\alpha u\right]_{y=-W/2} \mathrm{d}z + \int_{-W/2}^0 \tau_{base} \frac{\partial u(y,0)}{\partial y} \mathrm{d}y. \qquad \text{(B3)}$$

To calculate the two integrals in (B3) we need to know u within the ice stream. An approximate evaluation can be produced using a simple one-dimensional model with a constant basal stress τ_{base} beneath the ice stream. Assuming that τ_{xy} and u are functions of y alone we integrate the equation for mechanical equilibrium from $z = 0$ to $z = H$, arriving at

$$\frac{\mathrm{d}\tau_{xy}}{\mathrm{d}y} = -\left(\rho g \sin\alpha - \frac{\tau_{base}}{H}\right) \quad , \quad \dot{\epsilon}_{xy} = A\tau_{xy}^n\,, \qquad \text{(B4)}$$

where it may be noted that the first of these is exact if we reinterpret τ_{xy} as its average over the thickness H in the z direction. This average becomes arbitrarily larger than the average of τ_{xz} as W/H becomes increasingly large. In that same limit, $\dot{\epsilon}_{xy}$ becomes much larger than $\dot{\epsilon}_{xz}$, and the flow law reduces to the second equation. Treating the problem in that large W/H limit, we integrate outwards from the stress free boundary at $y = -W/2$ to calculate $\tau_{xy}(y)$ and hence the strain-rate profile

$$\frac{\mathrm{d}u}{\mathrm{d}y} = -2A\left(\rho g \sin\alpha - \frac{\tau_{base}}{H}\right)^n \left(y + \frac{W}{2}\right)^n. \qquad \text{(B5)}$$

To create the single boundary condition needed to integrate this equation we assume that the downstream velocity vanishes at the margin, as is appropriate to the large W/H limit, and find

$$u = \frac{2A}{n+1}\left(\rho g \sin\alpha - \frac{\tau_{base}}{H}\right)^n \left[\left(\frac{W}{2}\right)^{n+1} - \left(y + \frac{W}{2}\right)^{n+1}\right]. \qquad \text{(B6)}$$

The boundary condition used here is an approximation since the velocity field in the vicinity of the margin will be a function of both y and z, and will not completely vanish. However, comparing the predictions for velocity in the center of the ice stream from equation (B6) and two-dimensional computational models we find that in the limit $H \ll W/2$ equation (B6) is the asymptotic limit of such models.

Using the one-dimensional model to evaluate J_{tip}, which relies only on the value of u at the center of the ice stream, eq. B3 gives

$$\frac{J_{tip}}{2} = \frac{2AH}{n+1}\left(\rho g \sin\alpha - \frac{\tau_{base}}{H}\right)^{n+1} \left(\frac{W}{2}\right)^{n+1} \qquad \text{(B7)}$$

Defining the average lateral shear stress at the margins and the corresponding equivalent strain rate

$$\tau_{lat} = \left(\rho g \sin\alpha - \frac{\tau_{base}}{H}\right)\frac{W}{2} \quad , \quad \dot{\epsilon}_{lat} = A\tau_{lat}^n. \qquad \text{(B8)}$$

we can simplify the equation for J_{tip} to

$$J_{tip} = \frac{4H}{n+1}\tau_{lat}\dot{\epsilon}_{lat} \qquad \text{(B9)}$$

when $W \gg H$.

Tables

Table 1. Overview of the notation used in this study.

Symbol	Variable	Unit
a	surface accumulation rate of ice	$\mathrm{m\,yr^{-1}}$
A	temperature-dependent creep parameter	$\mathrm{s^{-1}\,Pa^{-3}}$
α	inclination angle	rad
c	specific heat of ice	$\mathrm{J\,kg^{-1}\,K^{-1}}$
c_1	empirical forefactor	$\mathrm{J\,kg^{-1}\,K^{-1}}$
c_2	empirical forefactor	$\mathrm{J\,kg^{-1}\,K^{-2}}$
d	grain size	mm
E	enhancement factor	
$\dot{\boldsymbol{\epsilon}}$	strain rate tensor	$\mathrm{yr^{-1}}$
$\dot{\epsilon}_D$	strain resulting from diffusional creep	$\mathrm{yr^{-1}}$
$\dot{\epsilon}_E$	effective strain rate	$\mathrm{yr^{-1}}$
$\dot{\epsilon}_G$	strain resulting from Glen's Law	$\mathrm{yr^{-1}}$
$\dot{\epsilon}_{lat}$	average shear strain at the margin	$\mathrm{yr^{-1}}$
F	variable used to calculate transition point stress field	m
g	gravitational acceleration	$\mathrm{m\,s^{-2}}$
G	Geothermal heat flux at the ice sheet base	$\mathrm{m\ W\,m^{-2}}$
Γ	curve along which J-integral is evaluated	
Γ_{tip}	curve through transition point stress field	
Γ_{far}	curve around border of domain	
H	ice sheet thickness	m
H_m	height of the temperate zone	m
J_{tip}	J-integral evaluated along Γ_{tip}	$\mathrm{J\,m^{-2}\,yr^{-1}}$
k	thermal conductivity of ice	$\mathrm{W\,m^{-1}\,K^{-1}}$
k_1	empirical factor	$\mathrm{W\,m^{-1}\,K^{-1}}$
k_2	empirical factor	$\mathrm{K^{-1}}$
k_B	Boltzmann constant	$\mathrm{m^2 kg\,s^{-2}\,K^{-1}}$
L	latent heat per unit mass	$\mathrm{J\,kg^{-1}}$
$\dot{m}$	melt rate per unit volume	$\mathrm{kg\,s^{-1}\,m^{-3}}$
n	exponent in ice rheology	
$\mathbf{n}$	unit normal vector to Γ	
μ	effective viscosity of ice	Pa s
μ_w	viscosity of water	Pa s
Ω	molecular volume	$\mathrm{m^3}$
ϕ	angle between principal strain rate direction and z	rad
Φ	strain energy density analog	$\mathrm{Pa\,yr^{-1}}$
q	meltwater flux	$\mathrm{m\,s^{-1}}$
q_{base}	meltwater flux at the bed	$\mathrm{m\,s^{-1}}$
q_{temp}	meltwater flux in the temperate zone	$\mathrm{m\,s^{-1}}$
Q	activation energy	$\mathrm{J\,mol^{-1}}$

Symbol	Variable	Unit
r	radial distance from the singularity	m
R	gas constant	$\mathrm{J\,K^{-1}\,mol^{-1}}$
ρ	density of ice	$\mathrm{kg\,m^{-3}}$
ρ_w	density of water	$\mathrm{kg\,m^{-3}}$
s	arc length of curve Γ	m
T	temperature	C
T_{melt}	melting temperature of ice	C
T_h	temperature adjusted for melting point depression	K
T^*	cutoff temperature in Glen's Law	K
$\boldsymbol{\tau}$	stress tensor	Pa
τ_E	effective stress	Pa
τ_{lat}	average shear stress at the margin	Pa
τ_{base}	basal shear stress	Pa
θ	angle from the base of the ridge	rad
u	downstream velocity component	$\mathrm{m\,s^{-1}}$
v	transverse velocity component	$\mathrm{m\,s^{-1}}$
v_0	speed of lateral margin migration	$\mathrm{m\,s^{-1}}$
v_{out}	velocity boundary condition in local model	$\mathrm{m\,s^{-1}}$
w	vertical velocity component	$\mathrm{m\,s^{-1}}$
W	ice stream width	m
x	downstream cartesian coordinate	m
X	variable used to calculate transition point stress field	m
ξ	dummy integration variable used to define Φ	
y	transverse cartesian coordinate	m
z	vertical cartesian coordinate	m